Geophysical Journal International

Geophys. J. Int. (2011) **187,** 1725–1742 doi: 10.1111/j.1365-246X.2011.05238.x

Asymmetric shallow mantle structure beneath the Hawaiian Swell—evidence from Rayleigh waves recorded by the PLUME network

Gabi Laske,[1] Amanda Markee,[1] John A. Orcutt,[1] Cecily J. Wolfe,[2] John A. Collins,[3] Sean C. Solomon,[4] Robert S. Detrick,[3] David Bercovici[5] and Erik H. Hauri[4]

[1]*Institute of Geophysics and Planetary Physics, University of California San Diego, La Jolla,* CA 92093-0225, *USA. E-mail: glaske@ucsd.edu*
[2]*Hawaii Institute of Geophysics and Planetology, University of Hawaii at Manoa, Honolulu,* HI 96822, *USA*
[3]*Department of Geology and Geophysics, Woods Hole Oceanographic Institution, Woods Hole,* MA 02543, *USA*
[4]*Department of Terrestrial Magnetism, Carnegie Institution of Washington, Washington,* DC 20015, *USA*
[5]*Department of Geology and Geophysics, Yale University, New Haven,* CT 06520, *USA*

Accepted 2011 September 16. Received 2011 September 10; in original form 2011 January 29

SUMMARY

We present models of the 3-D shear velocity structure of the lithosphere and asthenosphere beneath the Hawaiian hotspot and surrounding region. The models are derived from long-period Rayleigh-wave phase velocities that were obtained from the analysis of seismic recordings collected during two year-long deployments for the Hawaiian Plume-Lithosphere Undersea Mantle Experiment. For this experiment, broad-band seismic sensors were deployed at nearly 70 seafloor sites as well as 10 sites on the Hawaiian Islands. Our seismic images result from a two-step inversion of path-averaged dispersion curves using the two-station method. The images reveal an asymmetry in shear velocity structure with respect to the island chain, most notably in the lower lithosphere at depths of 60 km and greater, and in the asthenosphere. An elongated, 100-km-wide and 300-km-long low-velocity anomaly reaches to depths of at least 140 km. At depths of 60 km and shallower, the lowest velocities are found near the northern end of the island of Hawaii. No major velocity anomalies are found to the south or southeast of Hawaii, at any depth. The low-velocity anomaly in the asthenosphere is consistent with an excess temperature of 200–250 °C and partial melt at the level of a few percent by volume, if we assume that compositional variations as a result of melt extraction play a minor role. We also image small-scale low-velocity anomalies within the lithosphere that may be associated with the volcanic fields surrounding the Hawaiian Islands.

Key words: Mantle processes; Surface waves and free oscillations; Seismic tomography; Oceanic hotspots and intraplate volcanism; Pacific Ocean.

1 INTRODUCTION

Hawaii and its associated chain of islands and seamounts have long been regarded as the archetypal example of an intraplate hotspot that is located above a deep-rooted mantle plume (Wilson 1963; Morgan 1971). In the classical plume model, hot mantle material ascends nearly vertically within a more viscous surrounding mantle, before stagnating and 'pancaking' beneath the rigid lithosphere. By this hypothesis, buoyant plume-fed asthenosphere heats and uplifts the overlying lithosphere and gives rise to an elongated bathymetric swell as shallow plume material is dragged downstream by the overriding plate (Davies 1988; Olson 1990; Sleep 1990; Wessel 1993; Phipps Morgan *et al.* 1995). Alternative explanations for the Hawaiian hotspot have challenged the plume hypothesis. Foremost among these is the suggestion that a plate moving on an oblate Earth experiences extensional stresses (Turcotte & Oxburgh 1973) that cause the plate to fracture, allowing for the passive ascent of magma from the asthenosphere and age-progressive volcanism (Natland & Winterer 2005).

Hawaii's isolated location, far from plate boundaries, provides a unique opportunity to test basic hypotheses for the origin of hotspot volcanism (e.g. Ribe & Christensen 1999). But its midplate location, surrounded by a deep-ocean environment, has also proven an obstacle to the collection of diagnostic geophysical observations.

Identifying the dominant cause of the Hawaiian bathymetric swell has also remained elusive. Proposed mechanisms include thermal rejuvenation (Detrick & Crough 1978), dynamic support (Watts 1976), thermal erosion (Li *et al.* 2004), compositional buoyancy (Jordan 1979), and hybrids of these ideas (Laske *et al.* 2007). Early heat flow measurements along the Hawaiian Swell

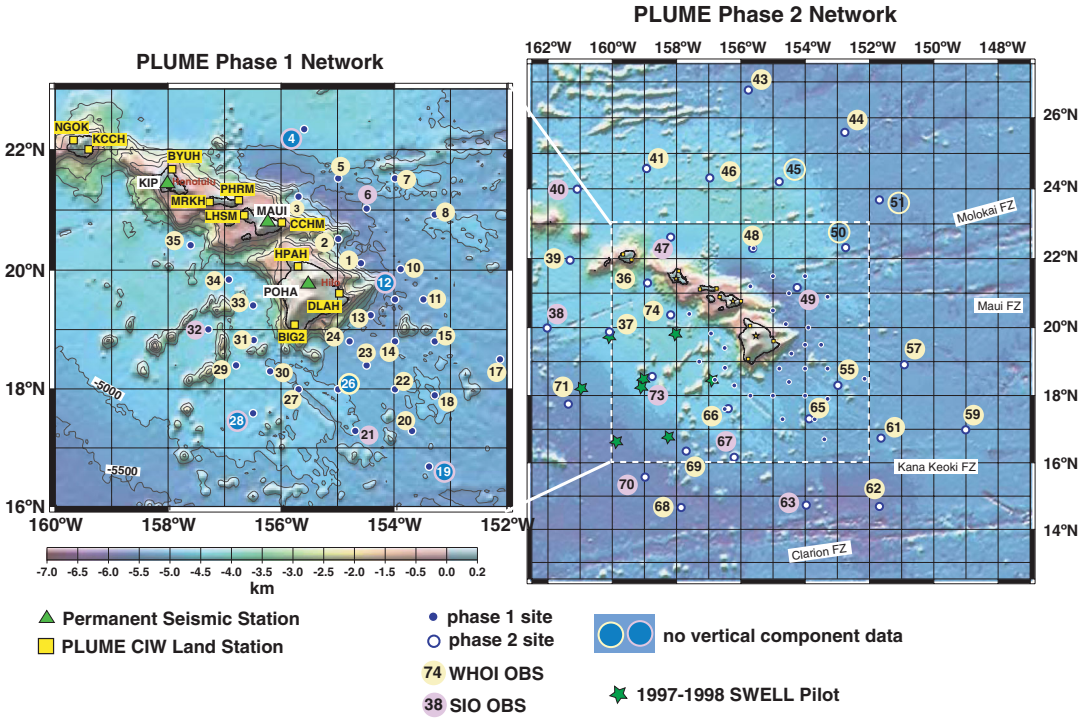

Figure 1. Site locations of the two one-year deployment phases of the Hawaiian PLUME project. Also shown are sites of permanent stations of global seismic networks relevant to this study. Station KIP (Kipapa, Oahu) is jointly operated by GEOSCOPE and the U.S. Geological Survey (USGS), POHA (Pohakuloa, Hawaii) by the USGS, and MAUI by GEOFON. Phase 1 (left-hand side) operated from 2005 January through 2006 January and phase 2 (right-hand side) from 2006 April through 2007 June. Only the recovered OBSs are shown; a total of 11 OBSs were lost. The complete deployment layout can be found in Laske *et al.* (2009a). Open numbered circles mark instruments with a loss of data for the differential pressure gauge (DPG) and/or vertical-component seismometer. Green stars mark the sites of the 1997–1998 SWELL pilot array (Laske *et al.* 1999).

appeared to support the thermal rejuvenation model (von Herzen *et al.* 1982), but subsequent measurements across the swell did not show the high heat flow values expected near the center of the swell. It was suggested by von Herzen *et al.* (1989) that dynamic support must also play a role. More recently, Harris & McNutt (2007) found that some heat flow data may be biased low as a result of hydrothermal circulation in the crust, so that any signal from thermal rejuvenation may be muted along the Hawaiian chain.

Regional seismic studies have so far yielded conflicting results. Single-path surface wave studies using the two-station method along the Hawaiian Islands found no evidence for lithospheric thinning (Woods *et al.* 1991; Woods & Okal 1996; Priestley & Tilmann 1999). Maupin (1992) argued, however, that single-path ray-theory methods fail to account for effects caused by surface waves trapped along a narrow low-velocity channel that may exist along the chain, if the Pacific Plate drags hot plume-derived asthenosphere material downstream. Among the proposed mechanisms for the Hawaiian Swell, only compositional buoyancy predicts high seismic velocities in the upper mantle near Hawaii. Katzman *et al.* (1998) reported such an anomaly near the end of a corridor between Fiji/Tonga and Hawaii. Their result, however, is not consistent with more recent regional studies around Hawaii that provided images of upper mantle low-velocity anomalies (Tilmann *et al.* 2001; Wolfe *et al.* 2002; Laske *et al.* 2007). Regional receiver-function studies suggested a thinning of the transition zone to the southwest of the island of Hawaii (Li *et al.* 2000; Collins *et al.* 2002), a zone of very low shear velocities beneath the island of Hawaii at 130 km and greater depth (Li *et al.* 2000; Wölbern *et al.* 2006), and a thinning of the lithosphere downstream of Hawaii (Li *et al.* 2004). Most of these studies relied solely on land seismic stations, and data coverage was lacking at key locations in all of these studies to fully assess upper mantle structure.

The Hawaiian Plume-Lithosphere Undersea Mantle Experiment (PLUME) (Laske *et al.* 2009a) involved a large deployment of ocean-bottom and land seismometers to address these questions. The experiment drew upon the experience gained during the PELENET experiment (Wolfe *et al.* 2002), the Seismic Wave Exploration in the Lower Lithosphere (SWELL) pilot experiment (Laske *et al.* 2007), and the Ocean Seismic Network pilot experiment (Collins *et al.* 2002). During the field campaign, which involved two year-long deployments of broad-band seismometers between 2005 January and 2007 June, 73 sites were occupied on the ocean floor and 10 on the Hawaiian Islands (Fig. 1). Seafloor instruments were provided and deployed by the Woods Hole Oceanographic Institution (WHOI) and the Scripps Institution of Oceanography (SIO) ocean-bottom seismometer (OBS) groups, both of which are institutional operators of the national OBS Instrument Pool (OBSIP) supported by the U.S. National Science Foundation. Land instruments were deployed and operated by the Carnegie Institution of Washington (CIW). The PLUME network was complemented by permanent seismic observatory stations KIP (Kipapa, Oahu), POHA (Pohakuloa, Hawaii) and MAUI (Maui). All seismic data collected during the PLUME field campaign are now available at the Incorporated Research Institutions for Seismology (IRIS) Data Management Center. This study presents results from the analysis of Rayleigh waves recorded across the PLUME network at frequencies between 10 and 50 mHz.

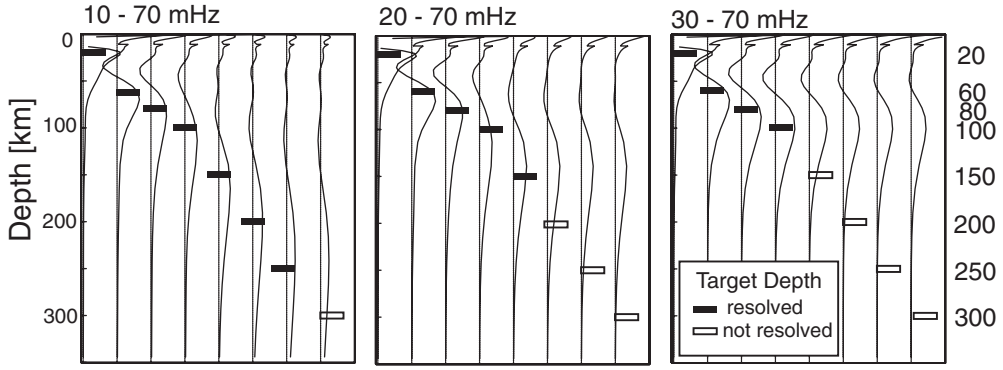

Figure 2. Backus–Gilbert resolving kernels for Rayleigh waves over three frequency ranges and for a given model error of 1 per cent. The eight kernels display the recovery of a δ-function at eight given target depths in kilometres (indicated by the numbers on the right). Rayleigh-wave phase velocity data at frequencies 10 mHz and above are capable of recovering structure down to 250 km depth.

2 THE PLUME FIELD CAMPAIGN, INSTRUMENTATION AND PHASE MEASUREMENTS

A 500-km-wide OBS network of 35 sites, with station spacing of about 80 km, recorded continuously from 2005 January through 2006 January (PLUME phase 1), whereas an OBS network of 38 sites, over 1000 km wide and with station spacing of about 220 km, recorded from 2006 April through 2007 June (PLUME phase 2). Most of the 10 portable broad-band land stations on the islands operated for the entire duration of the field campaign. All stations were equipped with wide-band or broad-band sensors: the PLUME land stations featured a broad-band Wielandt-Streckeisen STS-2 (triaxial components, corner period at 120 s), the WHOI OBSs had a Güralp CMG-3T (orthogonal components, corner period at 120 s), and the SIO OBSs had a wideband Nanometrics Trillium 40 during phase 1 (triaxial components, corner period at 40 s) and a broad-band Nanometrics Trillium 240 (corner period at 240 s) during phase 2. Each OBS included a Cox-Webb differential pressure gauge (DPG) (Cox *et al.* 1984). The observatory stations operated a broad-band STS-2 (MAUI), a very broad-band STS-1 (KIP) and a very broad-band Geotech/Teledyne KS54000 borehole seismometer (POHA). Vertical-component seismometer data comprise the primary data set for this study.

All stations recorded continuously at a variety of sampling rates: the WHOI instruments recorded at 1 Hz, in addition to 40 Hz (seismometers) and 20 Hz (DPG). The SIO instruments recorded at 31.25 Hz, and the CIW land stations recorded at 20 Hz. The observatory stations provide data at 1 Hz as well as other sampling rates. For this study, we bandpass filtered and resampled all data to 0.992 Hz (SIO) and 1 Hz (all other stations).

Of the 32 OBSs recovered from phase 1, 27 instruments provided vertical-component data. The Güralp seismometer at station PL26 did not unlock, and the central processing unit (CPU) on the SIO instruments PL04, PL12, PL19 and PL28 reset to record only two horizontal components. The equipment at PL02 experienced an unintended channel swap involving the vertical component that was not detected until after data analysis for phase 1 was complete. Of the 30 recovered OBSs from phase 2, 27 provided useful vertical-component data. Station PL40 also experienced an unintended channel swap, which was detected and rectified during data processing. Two of the three remaining sites (PL45, PL50, PL51) provided seismic signals on the DPGs but not on the vertical seismometer components. These stations are excluded from analysis.

A Backus–Gilbert resolution analysis (Backus & Gilbert 1968) reveals that Rayleigh wave phase velocity measured between 10 and 70 mHz is adequate to constrain shear velocity, V_S, to depths of at least 200 km (Fig. 2). Such an analysis explores how well the data can recover an anomaly in the shape of a δ-function placed at a target depth using the optimal linear combination of data. We chose to perform this test with the condition that the model errors be no larger than 1 per cent. The trade-off between the desired model error and the width (or spread) of the recovered δ-function controls the minimum depth range over which a structure is smeared by the modelling. Rayleigh wave sensitivity reaches deeper than 200 km (Fig. 3), but recovered δ-functions tend to spread over a depth range

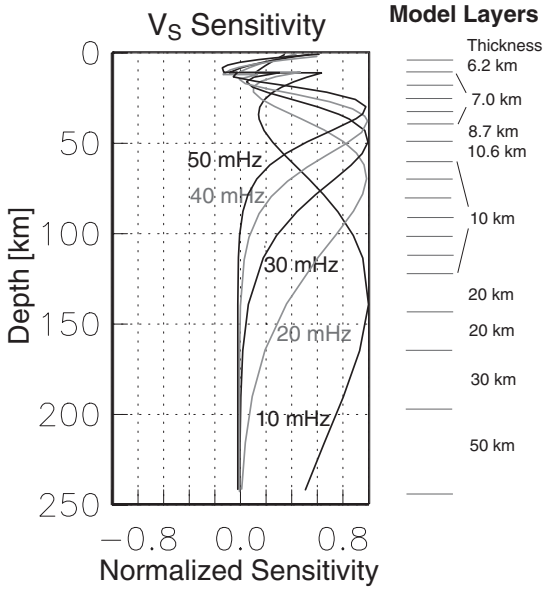

Figure 3. Left-hand side: Rayleigh-wave phase velocity sensitivity to shear velocity structure, V_S, as function of depth, z, shown at five frequencies. At a given frequency, the corresponding kernel is multiplied by the shear velocity structure and integrated over depth to obtain local phase velocity. The kernel for 10 mHz peaks at 140 km depth, but the combination of all frequencies gives the data set sensitivity to structure at much greater depths (see text for details). The kernels are normalized for better display. The maximum of the 50 mHz kernel is about 20 times larger than that of the 10 mHz kernel. Right-hand side: Geometry of the 17-layer velocity model used to represent shear velocity structure. The top and bottom layers are used to reduce the effects of bias from unresolved structure above and below our target depth range.

larger than ±50 km. A condition for good recovery in this test is that the data errors are consistently small across all frequencies, but in the data analysed here the errors at frequencies less than 20 mHz tend to become larger, so that the test results for deep structure somewhat overestimate resolution. Although it is straightforward to attain good depth resolution with observations on land, it has been questioned whether ocean noise hampers the observation of 10 mHz surface waves on the seafloor (e.g. Webb 1998). Even with data restricted to frequencies of 20 mHz and above, recovery of structure to depths near 150 km is possible, though imaging capabilities at depths much greater than 100 km deteriorate notably when the bandwidth is limited to frequencies of 30 mHz and above. Fortunately, such restrictions on bandwidth are rarely found in our PLUME data set. To suppress sensitivity to crustal structure, we limit our data analysis to frequencies less than 50 mHz.

Following the methodology of our SWELL pilot study (Laske *et al.* 1999, 2007), we selected moderately large, shallow teleseismic earthquakes (surface wave magnitude $M_S \geq 5.3$; source depths $h_0 < 200$ km; epicentral distance $\Delta > 20^\circ$). The 1997–1998 SWELL pilot experiment provided a rich database, but the years of the PLUME field campaign, 2005–2007, provided even more suitable earthquakes. For phase 1, we analysed 194 events, more than twice as many as for the SWELL study. For phase 2, we included only the 164 largest events with $M_S \geq 6.0$. Although many of these events are associated with the great 2004 December 26 Sumatra–Andaman earthquake, the increased seismicity during the PLUME deployments was not restricted to the Indonesian subduction zone, and the azimuthal coverage easily reaches that of the SWELL study.

For the Rayleigh wave dispersion analysis, we employed the multitaper transfer-function technique of Laske & Masters (1996) to measure the frequency-dependent, path-averaged Rayleigh wave phase velocity between station pairs. This procedure involves the manipulation of spectra for which the phase typically changes quickly as a function of frequency. Due to the different sampling rates, the SIO phase spectra must be interpolated in a joint analysis with the spectra from the other stations, which can introduce a systematic bias. We therefore analysed these stations separately. Because only three phase-1 SIO stations (PL06, PL21 and PL32) provided vertical-component data and so contribute with only three dispersion curves to a data set using the two-station method, we did not include these in this initial study. The data from all other stations were corrected for nominal instrument responses prior to analysis. Transfer function measurements were taken between 10 and 50 mHz, with 0.5 mHz increments, giving 81 phase velocity data for each dispersion curve. We applied the multitaper approach of Thomson (1982), and used a set of orthogonal Slepian tapers (Slepian 1978) that provide an optimal compromise between frequency resolution and bias from noise contamination. Used in a jackknife procedure (Efron 1987), these tapers allow us to obtain formal measurement errors. In combination with a wealth of crossing paths, the two-station approach lets us best assess lateral variations across the PLUME network without having to resort to modelling structure outside of it. However, this approach restricts the use of earthquakes to those for which the source azimuth does not deviate greatly from the associated two-station great circle. Path-averaged phase velocities were determined for events for which this deviation is no more than 10°. Each dispersion curve was corrected for nominal off-great-circle deviation, as uncorrected velocities are biased high (a 10° deviation leads to a 1.5 per cent velocity bias).

3 RAYLEIGH WAVE PHASE VELOCITY ACROSS THE PLUME NETWORK

Since along-path dispersion can be affected by off-path heterogeneity, we prefer to interpret dispersion in the context of 3-D velocity structure and therefore refrain from in-depth interpretations of single two-station dispersion curves. It is nevertheless useful to outline the range of dispersion curves in the PLUME data set of 614 paths as is shown in Fig. 4. The phase velocities along two-station path PL34–PL03 are anomalously low, indicative of deep-seated low shear velocities. We can find a 1-D velocity model that fits these data adequately, though it exhibits extremely low velocities of, 3.85 km s^{-1} at depths greater than 150 km. The phase velocities along path PL27–PL17 are much higher. At frequencies above 15 mHz, they resemble predictions for old oceanic lithosphere, though data at frequencies above 40 mHz appear to require modifications to the crustal structure. Relatively low velocities at frequencies less than 25 mHz require anomalously low velocities in the asthenosphere to be well fit.

For initial consistency checks, it is useful to display the results for all two-station pairs in map view, as a function of frequency. Fig. 5 reveals adequate overall internal consistency of the data set, although there are some outliers with extremely high or low velocities. Measurement errors tend to become larger with decreasing frequency but largely remain below 0.05 km s^{-1} (approximately 1 per cent; Fig. 6). It is notable that two-station paths crossing a region to the west of the island of Hawaii tend to exhibit unusually low velocities, especially at around 20 mHz. This tendency in also evident in the data for 10 mHz, but that data set appears less internally consistent. At higher frequencies, this feature disappears. This observation indicates that a pronounced low-velocity anomaly exists at depths well greater than 50 km but does not continue to the surface.

Two principal strategies lead from here to a 3-D shear velocity model. The first strategy (approach A) follows the methodology of Laske *et al.* (2007) in which path-averaged 1-D velocity profiles are obtained from inversions of each path-averaged dispersion curve. In a second inversion for maps at a set of given depths, these 1-D models are then inverted for 3-D structure. This technique was applied in the SWELL pilot study (Laske *et al.* 1999, 2007) and was also used in the presentation of initial PLUME models (Markee *et al.* 2008; Laske *et al.* 2009b; Strader *et al.* 2009). It finds wide usage, in particular in waveform modelling such as the partitioned waveform modelling by Nolet (1990). Though leading relatively quickly to a 3-D model, and with overtone dispersion included implicitly in waveform modelling, this approach has several disadvantages: (1) it is somewhat cumbersome to propagate errors through the two inversions; (2) meaningful resolution and hypothesis tests are difficult to implement; (3) so, too, are data quality and misfit checks; and (4) corrections for bathymetry and crustal structure have to be applied to each of the 614 dispersion curves individually by integration over the two-station paths. In our preferred approach B, frequency-dependent maps of local phase velocity anomalies are constructed from the path-averaged dispersion curves. These maps are then inverted for 3-D shear velocity structure. It is nonetheless useful to inspect results from both approaches to identify the most robust features in the derived models. We therefore present the results from approach A in the Supporting Information but proceed with approach B from here on.

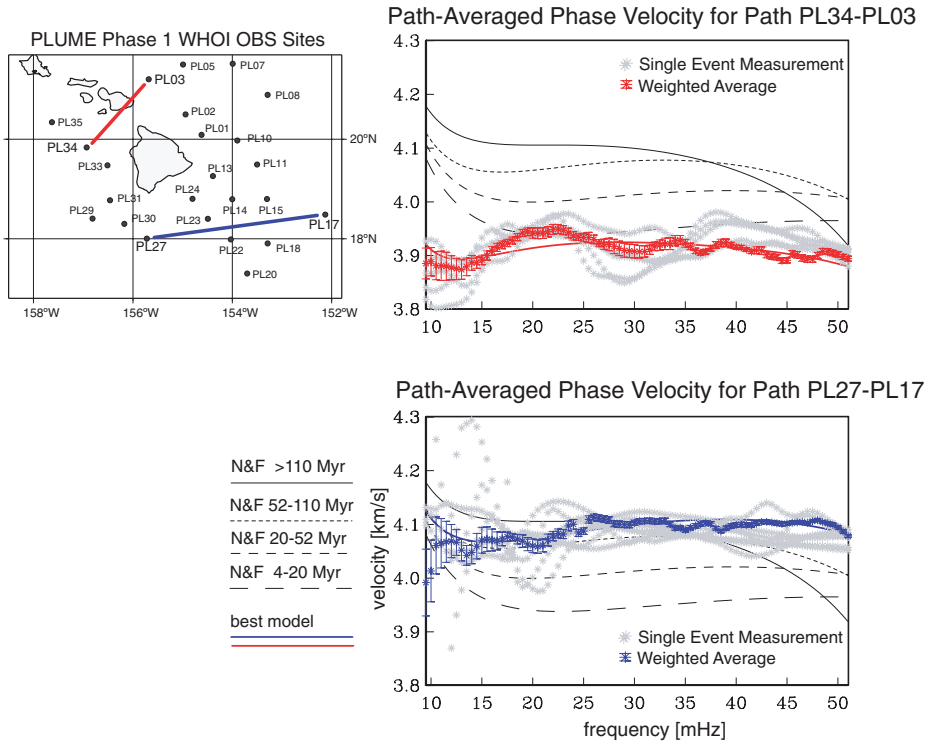

Figure 4. Path-averaged two-station dispersion curves for two station pairs. Path PL27–PL17, to the south of Hawaii, exhibits relatively high phase velocities, whereas path PL34–PL03, across Maui, has unusually low velocities. Solid lines mark predictions from a best-fitting 1-D velocity model. Predictions by Nishimura & Forsyth (1989) (N&F) for oceanic lithosphere of varying ages are also marked. The corresponding N&F 1-D models are displayed in Fig. 15. The age of the lithosphere surrounding Hawaii is 90–100 Myr.

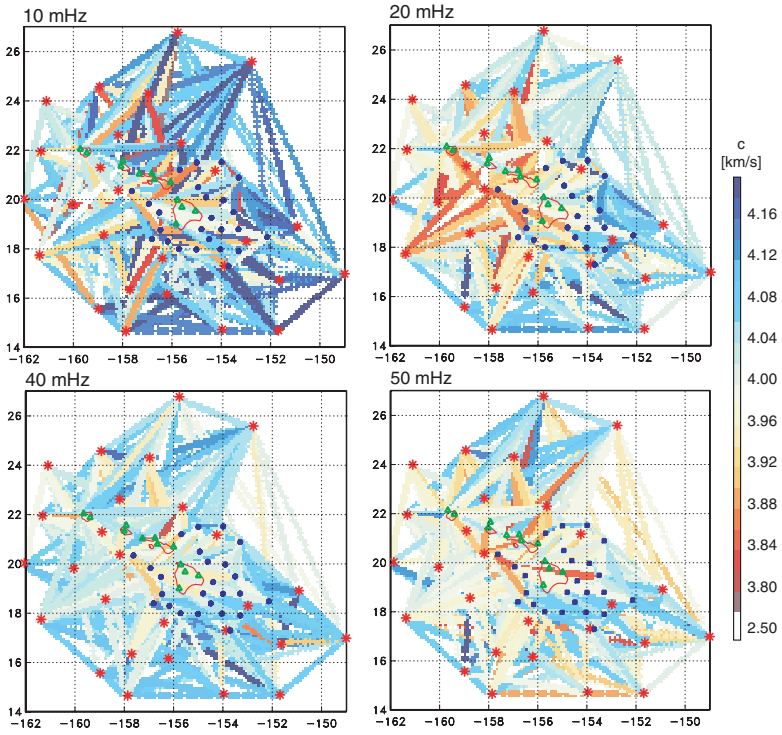

Figure 5. Path-averaged phase velocities across the PLUME network as functions of frequency. Overall, the data appear most internally consistent between 20 and 40 mHz. The most prominent feature in the maps is a low-velocity anomaly to the west of the island of Hawaii at frequencies of 20 mHz and below.

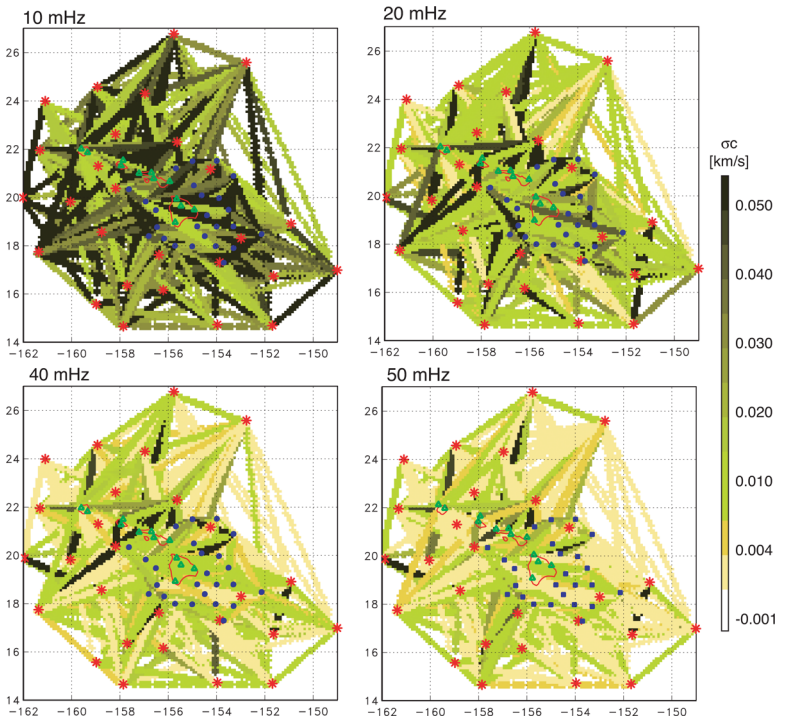

Figure 6. Errors for the path-averaged phase velocities shown in Fig. 5. Errors tend to increase with decreasing frequency.

4 MAPS OF LOCAL PHASE VELOCITY ANOMALIES

The 614 path-averaged dispersion curves were used as input in Occam's smoothed inversions (Constable *et al.* 1987) to solve for phase velocity maps at each of the 81 frequencies between 10 and 50 mHz. The phase velocity maps were defined in 13 × 13 1° cells, and we applied second-derivative smoothing in the inversions. In an Occam's smoothed inversion, we attempt to minimize the weighted sum of data misfit and model roughness (see Supporting Information for details). There is a trade-off between the two, with smoother models fitting the data less well. We found that properly weighting the data by the inverse of their squared errors is important. Drawing from our experience with global inversions, we also chose a minimum error threshold, because a minority of data with very small errors would otherwise dominate the inversions (see also Laske & Masters 1996). This problem also occurs in approach A but is more difficult to explore and control with that method. Resulting maps of local phase velocity anomaly are shown in Fig. 7 at four frequencies. These maps provide a much clearer initial picture of local structure than the maps of path-averaged phase velocities (Fig. 5). The corresponding maps of uncertainty estimates are shown in Fig. 8. The latter were obtained from inversions of the standard deviations of the path-averaged phase velocity curves. Cells not occupied by any paths have very small but non-zero uncertainties as a result of the lateral smoothing constraint imposed by the inversion (compare with Fig. 9). Despite relatively high hitcounts for cells around the island of Hawaii, uncertainties are relatively small for frequencies higher than 10 mHz, thereby documenting good internal consistency for paths crossing this region.

A pronounced low-velocity anomaly that is centred to the west of the islands is found in the 10 mHz map (Fig. 7). The magnitude of this anomaly lessens quickly with increasing frequency. This anomaly appears to be robust as the corresponding errors are relatively small. Consulting the sensitivity kernels in Fig. 3, we infer that the associated anomaly in V_S must reach deep into the asthenosphere but cannot continue to the surface, because otherwise this anomaly would be visible in the 50 mHz map. Relatively high velocities are found to the southeast of the islands. Small-scale features emerge in the 40 and 50 mHz maps that sample primarily the lithosphere and crust. Some of these anomalies coincide with past volcanism (Section 7). Some anomalies appear to collocate with seismic stations, which may suggest artefacts caused by malfunctioning stations. For example, a small low-velocity anomaly is found to the south of Oahu, near station PL73 (Fig. 1), particularly in the low-frequency maps. Repeat inversions without data from this station yield virtually identical maps, however, indicating that this anomaly is not the result of a problematic station. Similarly, a high-velocity anomaly near station PL17 to the southeast of Hawaii persists in the high-frequency maps after removing the data from that station. In this case, the amplitude is reduced by a factor of approximately two but remains in place. Somewhat intriguing is the large low-velocity region to the northeast of the island chain seen in the maps at higher frequencies. Data coverage is relatively poor in this area because of a lack of stations, but all paths crossing this region consistently exhibit low phase velocities (Fig. 5).

5 3-D SHEAR VELOCITY FROM PHASE VELOCITY MAPS

The resulting phase velocity maps were used as 'data' in an inversion for 3-D V_S structure (see Supporting Information for technical details). We performed Occam's smoothed inversions for 1-D V_S models in each of the 13 × 13 one-degree cells applying radial smoothing. Each 1-D model was parameterized by 17 layers of constant velocity, where the layer thickness increases with depth to reflect the degrading resolution (see Figs 2 and 3). As a starting model, we used a modified Nishimura & Forsyth (1989) (N&F) model for 52–110-Myr-old lithosphere (Laske *et al.* 2007) (see

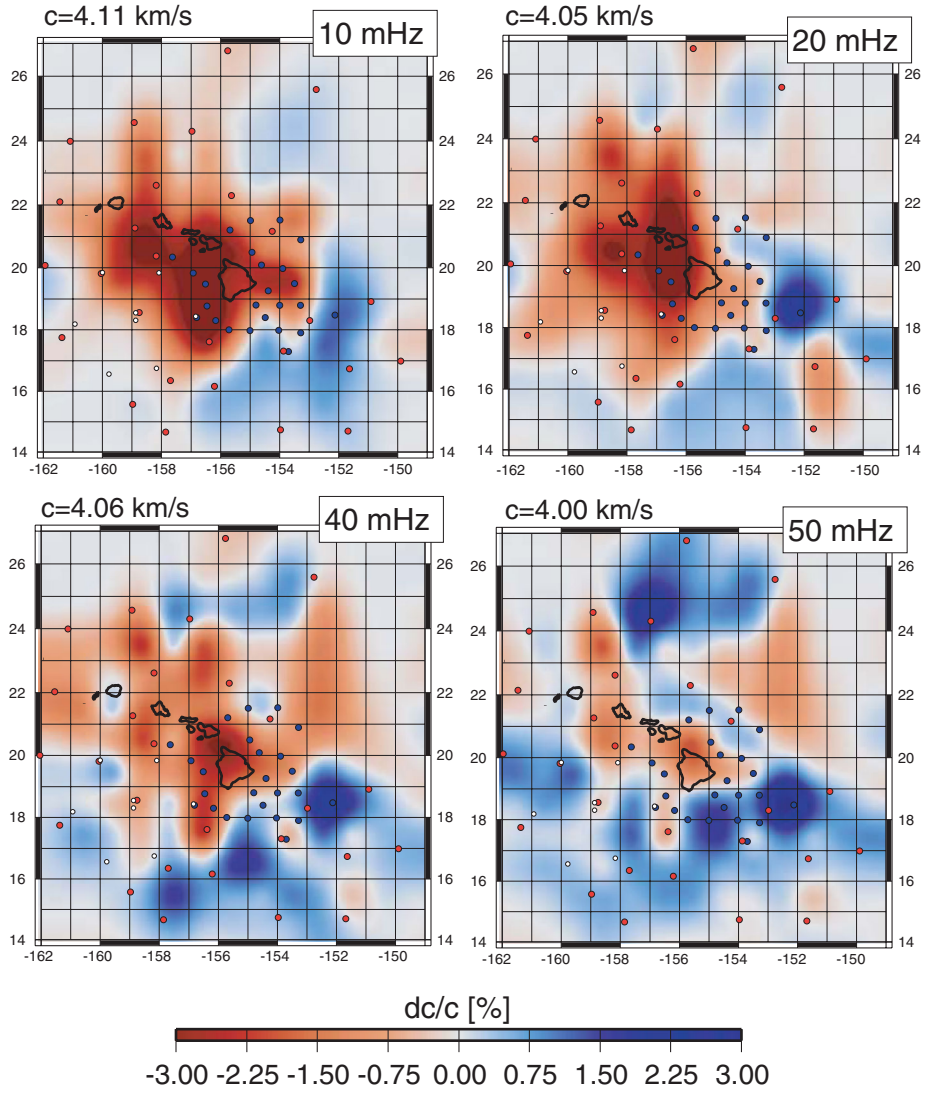

Figure 7. Maps of local phase velocity anomaly, *dc*/*c*, at four frequencies obtained from inversions of path-averaged phase velocity data (Fig. 5). The reference velocity for each map is given above each panel. It corresponds to the dispersion calculated for the modified Nishimura & Forsyth (1989) starting model for 52–100-Myr-old oceanic lithosphere. The complete collection of phase velocity maps comprises 81 maps at frequencies between 10 and 50 mHz. Different symbols mark the PLUME phase 1 (blue) and phase 2 (red) OBS sites. For reference and comparison with later figures, the sites of the SWELL pilot experiment are also shown (white).

Fig. 15). No lateral smoothing was used, since this was already applied in the inversions for phase velocity maps. As 'data errors' we used the uncertainties shown in Fig. 8. Formally, the data errors should be retrieved from the covariance matrices constructed in the inversions for phase velocity maps. This covariance approach yields larger errors for poorly sampled regions. Using such errors in the 1-D inversions allows resulting models to deviate markedly from the starting models at locations where no data constraints would justify such deviations. In contrast, with the approach chosen here, resulting models stay close to the starting model in poorly sampled regions. The final 3-D shear velocity model is presented in Fig. 10. Overall, features in the model are quite similar to those found in the model from approach A (Fig. A8), for which variations appear laterally smoother at shallow depths but rougher at greater depths.

A stable feature in the models from both approaches is the pronounced low-velocity anomaly to the west of Hawaii, at depths greater than 60 km. The bulk of this anomaly is laterally confined to lie within an area 100 by 200 km that is elongated in the north–south direction. The anomaly appears to connect with a smaller anomaly near a depth of 60 km that is centred between the islands of Hawaii and Maui. A weak, north–south-trending low-velocity anomaly to the northeast of the islands (at 152.5 ° W) is confined to depths less than 60 km. As discussed below, this particular anomaly finds support in the two-station dispersion data, but its large lateral extent is likely a result of imaging effects in a poorly resolved region. Small-scale low-velocity anomalies visible at a depth of 40 km extend downward but fade out quickly at depths greater than 60 km.

Although we restricted our data set to frequencies at and less than 50 mHz, some remaining sensitivity to crustal structure may affect the imaging of features to a depth as great as 80 km. To estimate the extent of these effects, we also performed inversions of maps that were corrected for crustal structure and bathymetry. The changes in the resulting models are very minor (compare to Fig. 11 and figures in the Supporting Information). In such models, features deeper than 40 km remain largely unchanged, though the amplitude of the large deep anomaly is somewhat reduced. This difference can likely

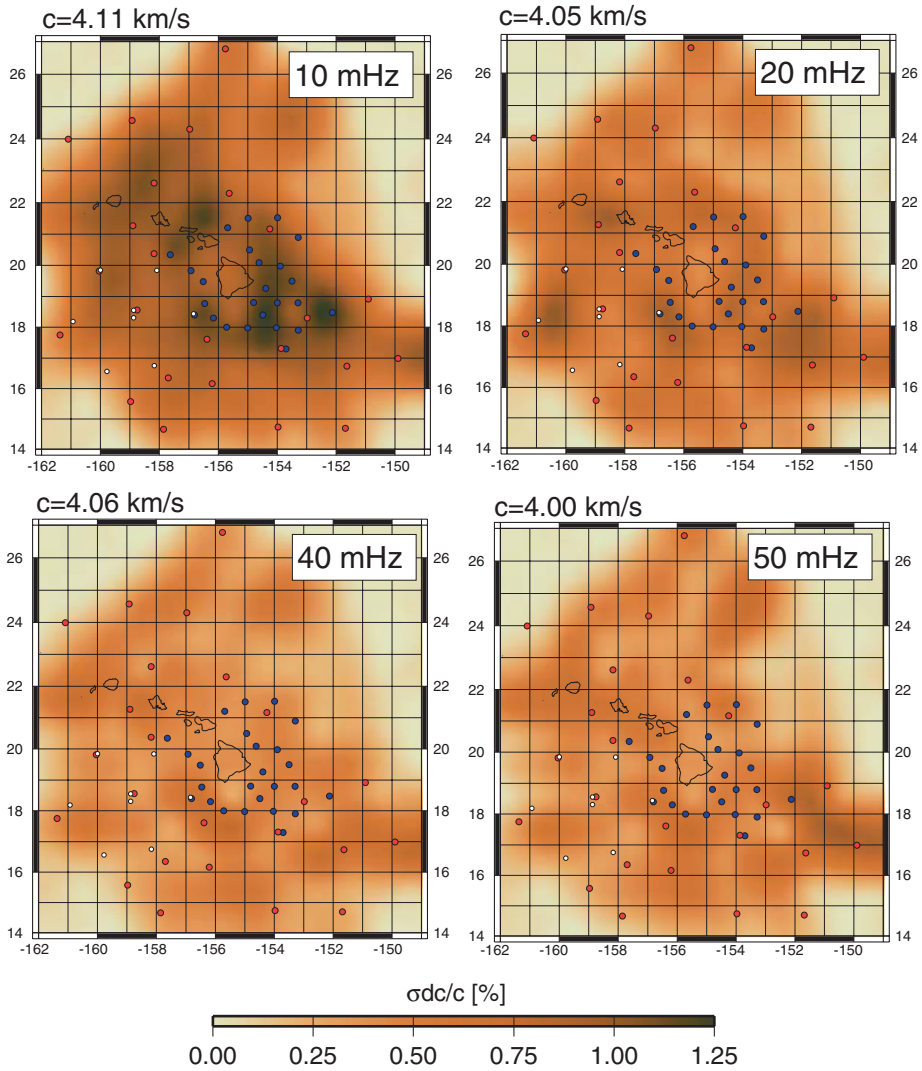

Figure 8. Estimates of uncertainty in local phase velocity, at the four frequencies shown in Fig. 7, obtained from inversions of the path-averaged phase velocity errors (Fig. 6). Percentage perturbations to the same reference velocities as in Fig. 7 are shown.

be offset by choosing the next rougher model along the trade-off curve between data misfit and model roughness.

5.1 Adding data from the SWELL pilot experiment

The shear velocity models obtained from inverting PLUME data (e.g. Fig. 10) exhibit low-velocity anomalies that reach well into the area covered by the SWELL pilot experiment (Laske *et al.* 2007) that used DPGs as sensors. There, we imaged lower shear velocities beneath the Hawaiian Swell that reached across the northeastern half of the SWELL network. The anomaly was apparent at all depths greater than 40 km, but the contrast between low on-swell and high off-swell velocities was most pronounced in the asthenosphere at depths near 100 km. In the V_S model shown here, the low-velocity anomalies in the asthenosphere appear to wrap around the centre of the SWELL network instead of spreading into it. We could argue that this may be the result of uneven path coverage (Fig. 9), but the maps from the SWELL V_S model also hint such a split (Laske *et al.* 2007).

We infer from this comparison that the data from these experiments are consistent despite the use of different sensors, and we include the SWELL data in a final set of inversions. As discussed in the next section, synthetic tests confirm that the 22 dispersion curves from the SWELL pilot study improve recovery of structure in the southwestern corner of the PLUME study area, at frequencies above 10 mHz (the SWELL data set includes frequencies at and above 11 mHz). The final model is displayed in Fig. 11. The addition of the SWELL data somewhat enhances the western extent of the low-velocity anomaly at depths between 60 and 120 km. The most notable change is that high-velocity anomalies to its west appear more pronounced and continuous, thereby forming an apron of high velocities around the island of Hawaii. These high velocities approximately coincide with off-swell deep seafloor (water depth greater than 5000 m).

6 SYNTHETIC TESTS

Synthetic tests are useful tools to evaluate the imaging fidelity of our data set and inversion technique. The ability to resolve subsurface structure depends on the path geometry, data errors, parameterization, and smoothing applied in the inversions. Since the resolution in the final V_S model is controlled by geometries and errors in

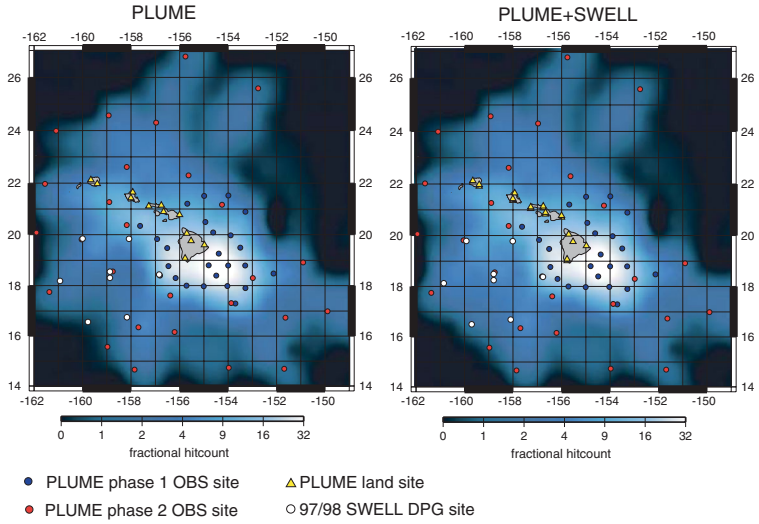

Figure 9. Two-station path coverage for phase velocity data at 40 mHz: (a) for the 614 paths of the PLUME network; (b) for the 636 paths including both the PLUME and the 1997 SWELL pilot networks. The contribution of each path to a 1° cell is determined by the length of the path segment within that cell. The value in each cell is the sum of the contributions of all paths to this cell. The absolute numbers on the colour scale are somewhat arbitrary and depend on how finely the paths are sampled (we chose 0.02°). Because of the large number of (crossing) paths from the phase-1 deployment, cells around the island of Hawaii are particularly well covered. Coverage diminishes toward the perimeter of the network and is relatively poor to the northeast of the islands, where several OBSs were not recovered (see Laske *et al.* 2009a, for details).

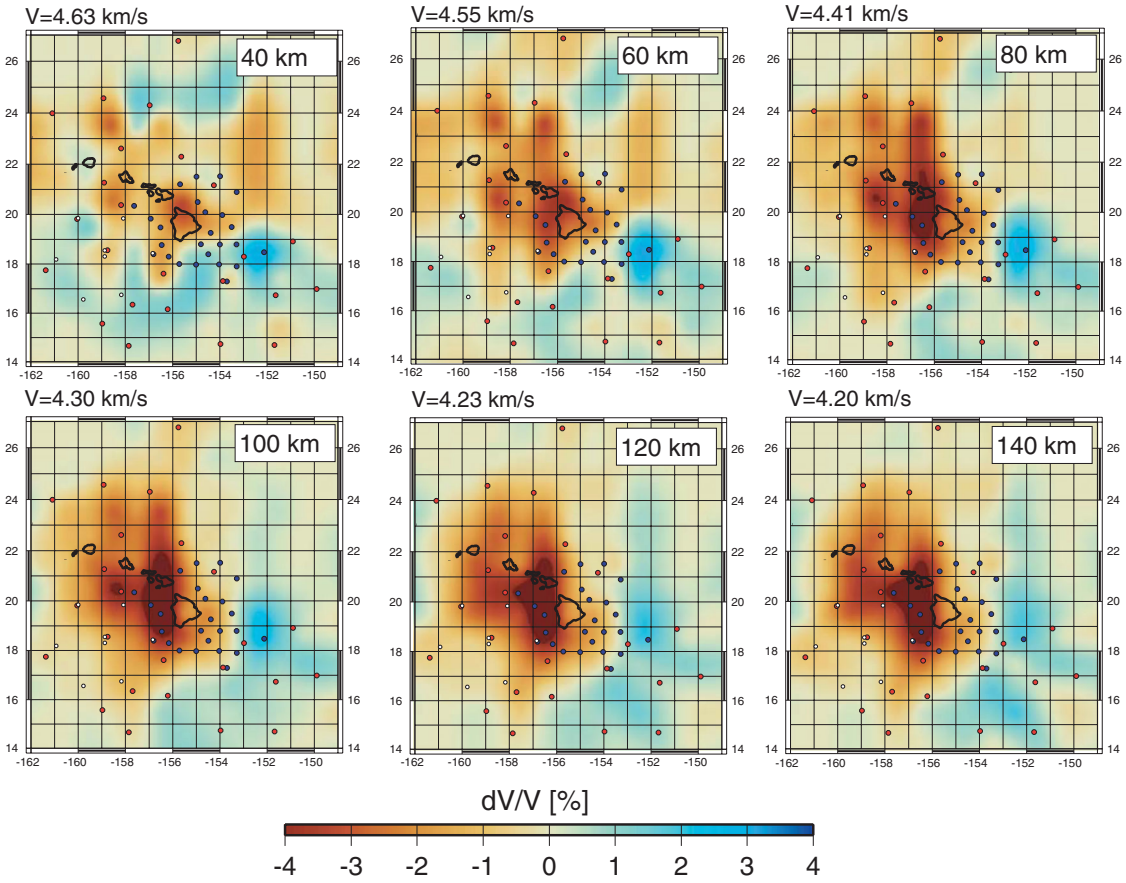

Figure 10. Model of shear velocity anomaly, dV_S/V_S, obtained from the inversion of PLUME data. For clarity in the panels, the subscript is omitted. The six panels show percentage perturbations to the reference model at depths between 40 and 140 km. The reference model is the modified N&F model for 52–100-Myr-old lithosphere (see text for details). The reference velocity at each depth is given above each panel. Different symbols mark the PLUME phase 1 (blue) and phase 2 (red) OBS sites. For reference, the sites of the SWELL pilot experiment are also shown (white). The phase velocity maps were not corrected for effects caused by bathymetry and crustal structure prior to the inversion.

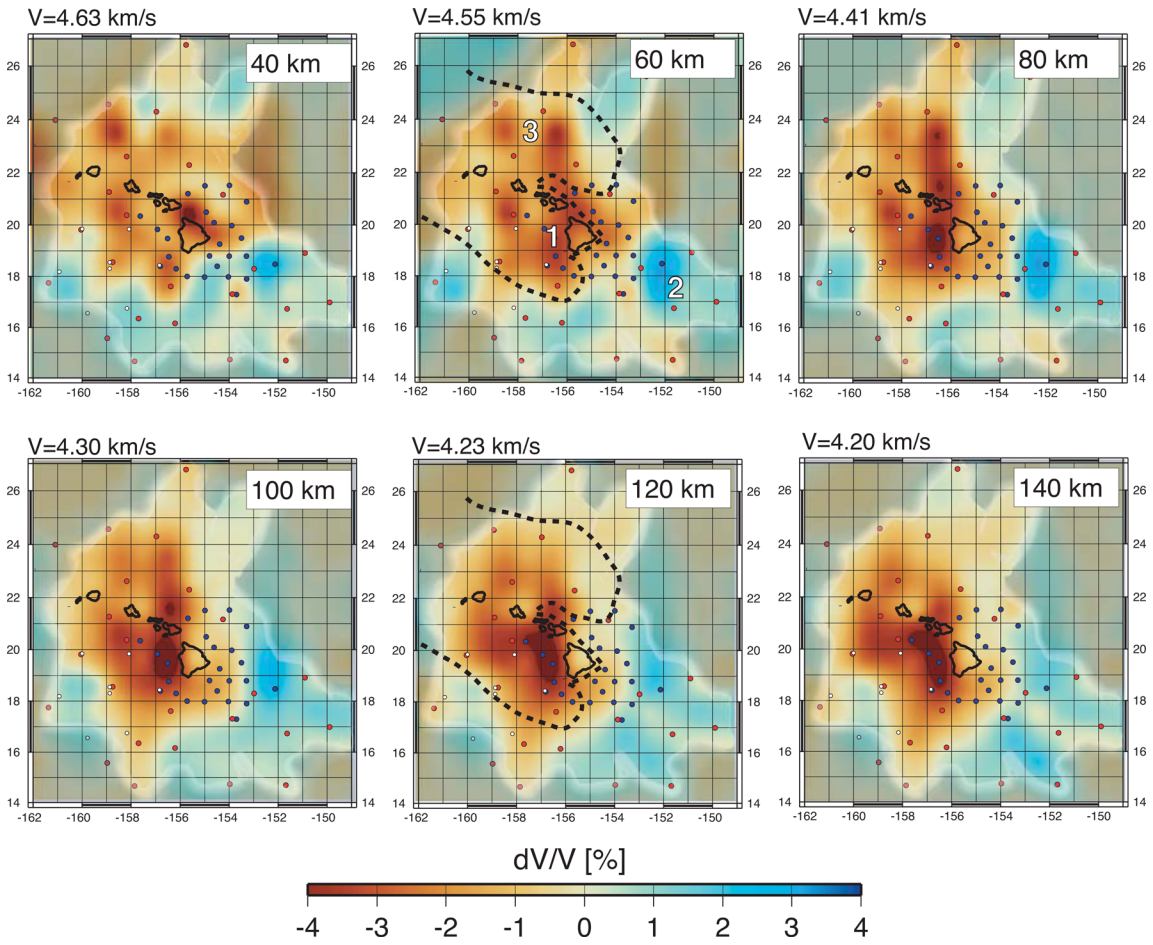

Figure 11. Model of shear velocity anomaly obtained from the inversion of both PLUME and SWELL data. See Fig. 10 for details. The input phase velocity maps were corrected for effects caused by bathymetry and crustal thickness prior to the inversion (see Supporting Information). The three numbers in the panel for 60 km mark the locations of the 1-D models of absolute shear velocity shown in Fig. 15. In the two middle panels, black dashed lines at 5000 m seafloor depth outline the Hawaiian Swell. Areas of reduced resolution are shaded over.

the input phase velocity maps, we present synthetic tests for these maps. We used the same constraints in the tests that we used in the inversions of the observations. The choice of suitable input models is a somewhat subjective process. Checkerboard tests are useful to obtain a quick overview. Here, we show results for the combined PLUME and SWELL data sets. Tests that include only PLUME data are presented in the Supporting Information.

The recovery of three input patterns, with a 5 per cent anomaly and different cell sizes, is shown in Fig. 12. The spatial recovery is best at frequencies between 35 and 45 mHz and degrades for lower and higher frequencies as the errors increase (see also Fig. 8). Large input squares, with dimensions of 300 km (upper row in Fig. 12), are recovered in most areas that are well-sampled by data (compare to Fig. 9). At frequencies of 30 mHz and higher, the amplitude of the recovered anomaly is typically above 4 per cent in cells with a relative hit count of 7 or higher. This corresponds to an amplitude recovery of 80 per cent or better in well-sampled regions. Even at 20 mHz, some cells in the output pattern have amplitudes greater than 4 per cent though the typically recovered amplitudes stay near 3 per cent (60 per cent amplitude recovery). At 10 mHz, the spatial recovery of larger input structures is possible out to at least 500 km from the islands, on both sides of the island chain, but the recovered amplitudes exceed 3 per cent in relatively few cells.

The area of best recovery of structure with dimensions of 200 km is within approximately 500 km of the island chain (middle row in Fig. 12), where the better recovery to the southwest than to the northeast reflects the better data coverage. Imaging fidelity is also high to the southeast of the island of Hawaii. Recovered amplitudes are slightly lower than for the larger input pattern, but most well-sampled cells have an amplitude recovery of 70 per cent or better. In some areas, it is numerically possible to recover structures on the scale of 1° (bottom row in Fig. 12). For 10-mHz waves, this scale is smaller than half the wavelength ($\lambda/2 \simeq 200$ km), so finite-frequency theory may be needed to interpret these data. Since a 1° cell also reflects the model parameterization, the recovery of structure of this dimension is penalized most in our smoothed inversions, and it is not surprising that amplitude recovery typically does not exceed 50 per cent.

Tests with isolated anomalies confirm that an anomaly close to the islands can be recovered spatially quite accurately at all frequencies (Fig. 13, bottom row). The highest recovered amplitude is 4.3 per cent (86 per cent amplitude recovery), with all four cells in the central anomaly of the output map having values of 3.3 per cent or higher (66 per cent amplitude recovery). An anomaly placed upstream from Hawaii (middle row) can also be recovered spatially, but signal is lost in the map at 10 mHz for distances markedly greater than 400 km. Amplitude recovery for the centre of this anomaly is

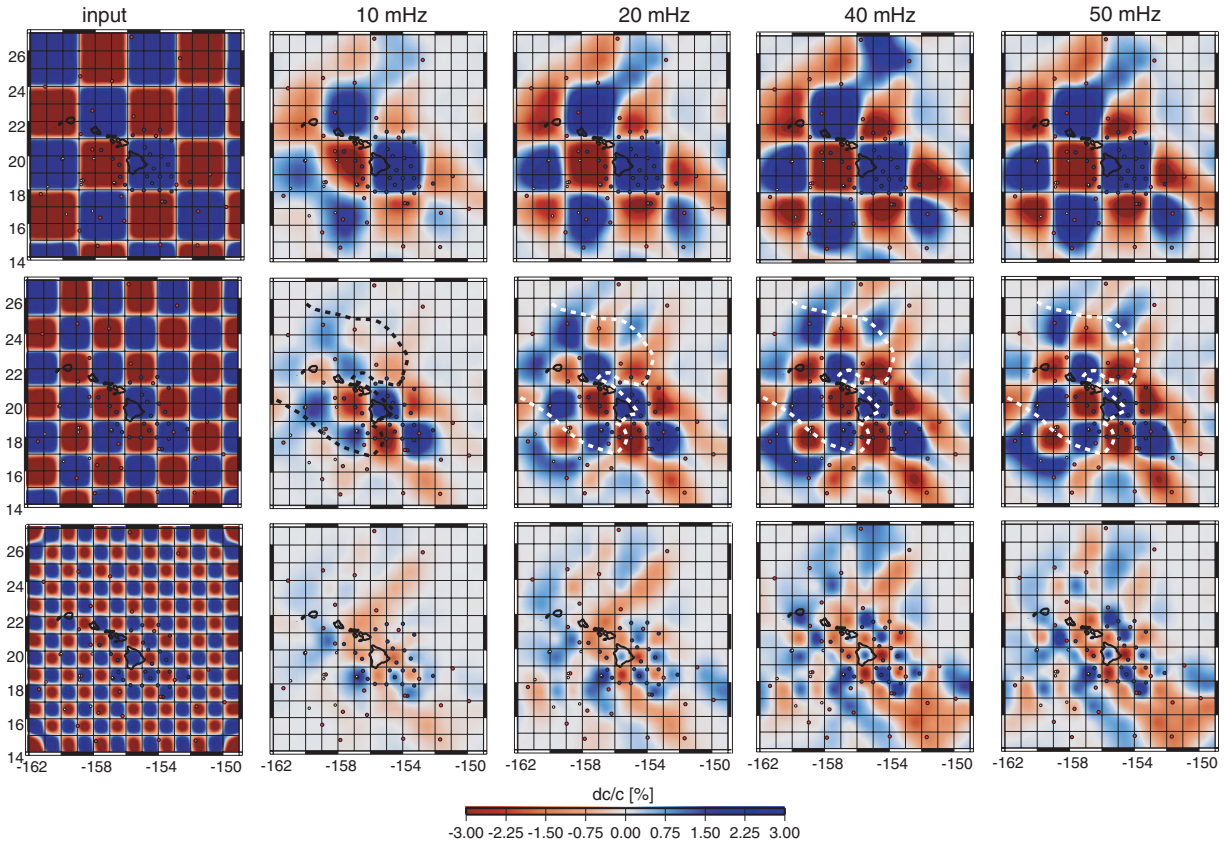

Figure 12. Checkerboard recovery tests for three input phase velocity maps with squares of varying size (left column), shown at four frequencies (the other four columns). Ray paths include those of the PLUME and SWELL data. The magnitude of the input anomaly is ±5 per cent. The size of the squares in the model on the bottom is 1°, which is the grid size in the parameterization. In the middle row of panels, dashed lines at 5000 m seafloor depth outline the Hawaiian Swell.

reduced, with an 80 per cent recovery in only one of the four central cells involved. An anomaly placed near the western edge (top row) appears to be recovered incompletely, particularly at 10 mHz, where its amplitude is grossly underestimated. At frequencies of 30 mHz or higher, the amplitude recovery of the center of this anomaly is 80 per cent or better in five of the nine involved cells.

The synthetic tests indicate that spatial recovery of small, 200-km-wide features is possible in well-sampled regions, with an amplitude recovery of 70 per cent or better. Slightly larger features have an amplitude recovery of 80 per cent or better. Amplitude recovery is markedly reduced at frequencies near 10 mHz, so velocity anomalies at depths greater than 150 km may be underestimated (compare with Figs 2 and 3). Since we limit the interpretation of our model to depths less than 150 km, we expect an amplitude recovery of 70 per cent or better in well-sampled regions, even in the upper asthenosphere, and for relatively small features. The amplitude recovery for larger features should be above 80 per cent.

7 DISCUSSION

7.1 Robust features in the V_S model

Relative to 52–110-Myr-old lithosphere, a broad region of anomalously low shear velocities beneath the Hawaiian Swell stands out in our images (Figs 11 and 14). Within this region, a strong, narrow low-velocity anomaly at depths greater than 80 km to the west of Hawaii is the most robust feature in our images. This feature continues well into the asthenosphere, to a depth of at least 140 km, as was partly evident in the prior SWELL study (Laske *et al.* 2007). Such an asymmetric low-velocity anomaly with respect to the island chain was also suggested by body-wave tomography (Wolfe *et al.* 2009, 2011). This region likely marks the supply route of hot, melt-rich and/or compositionally altered asthenosphere material. In their receiver function study, Wölbern *et al.* (2006) inferred a strong low-velocity anomaly at depths greater than 100 km directly beneath the island of Hawaii, which appears inconsistent with our results.

We can also rule out with confidence that strong low-velocity anomalies exist upstream from Hawaii within the lithosphere or asthenosphere. Instead, the Hawaiian Swell is surrounded by an area of high velocities at asthenospheric depths. Wolfe *et al.* (2009, 2011) interpreted this zone of high velocities as the parabola-shaped signature of downwelling mantle flow that surrounds a strong plume centre, as predicted by some mantle geodynamical models.

Anomalies shallower than 60 km tend to be isolated small-scale features. At these depths, the strongest anomaly is a low-velocity anomaly near the northern end of the island of Hawaii. This anomaly appears to shift westward with depth and likely connects to the deeper low-velocity anomaly to the west. Some of this shallow anomaly may be the result of enhanced magmatism and crustal thickening where the Molokai Fracture Zone intersects the island axis (Van Ark & Lin 2004). This scenario may also apply to the Maui Fracture Zone; see also Natland's and Winterer's comments following Laske *et al.* (2007). Including or ignoring corrections for

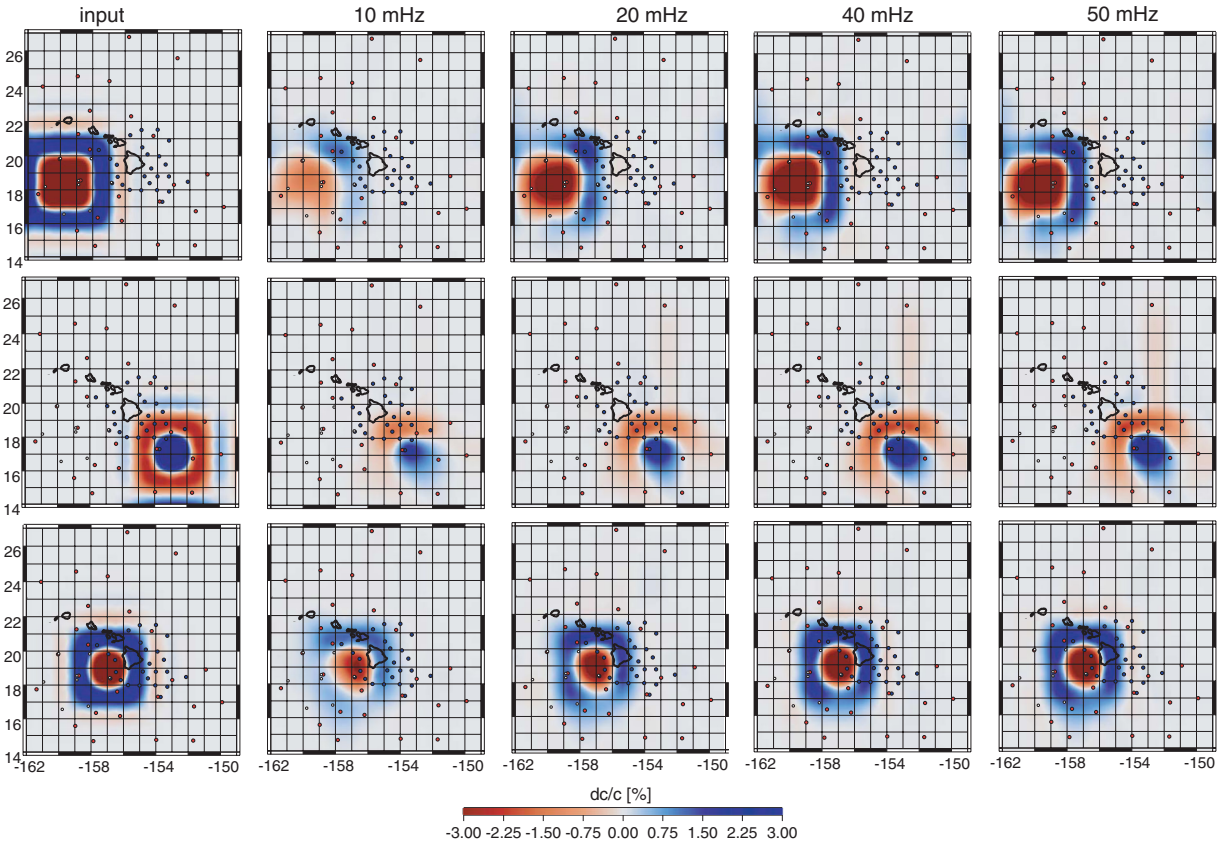

Figure 13. Recovery tests for isolated input anomalies at three different locations in a phase velocity map, shown at four frequencies. Ray paths include those of the PLUME and SWELL data. The magnitude of the input anomaly is 5 per cent, and the anomaly is surrounded by a 2.5 per cent anomaly of opposite sign.

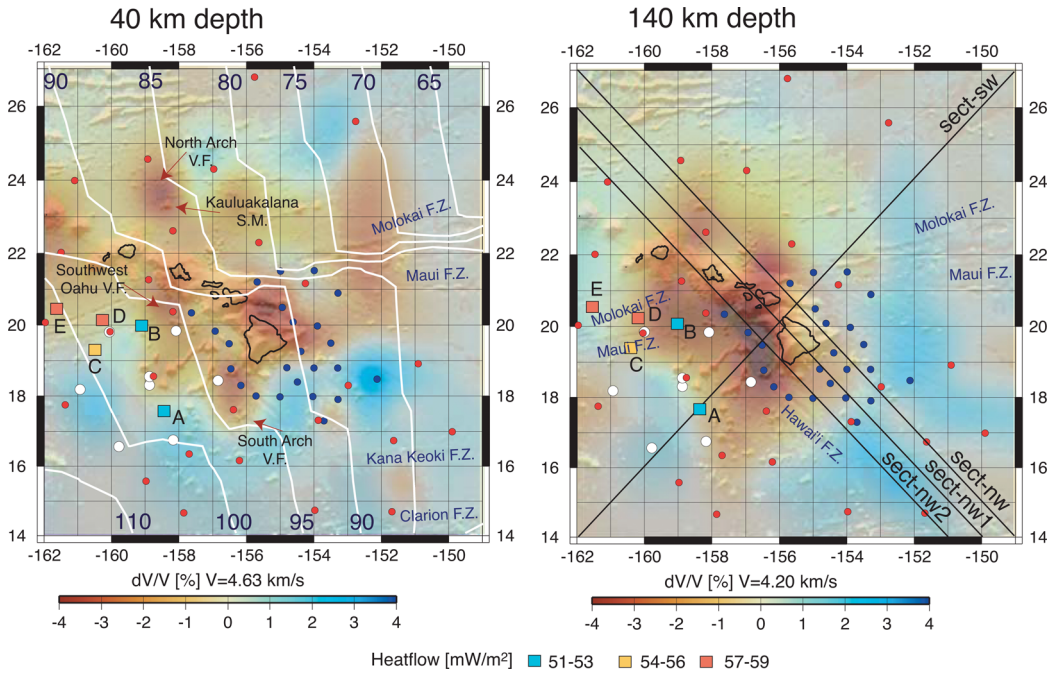

Figure 14. Two maps of the shear velocity model shown in Fig. 11, overlaid on grey-shaded bathymetric relief. White lines denote contours of crustal age in Myr from Müller *et al.* (2008). Colour-coded squares mark heat flow sites of von Herzen *et al.* (1982). Black lines mark the locations of the cross-sections shown in Fig. 16. The labels 'V.F.', 'S.M.' and 'F.Z.' stand for 'volcanic field,' 'seamount' and 'fracture zone.' See Fig. 7 for station symbols.

crustal effects and bathymetry does not move this anomaly notably (compare Figs 10 and 11). In a local body-wave study using data collected on the island of Hawaii, Tilmann *et al.* (2001) found low values of V_P at depths to 80 km beneath the entire island, but the lowest velocities were reported toward the northern end.

7.2 Possible causes for V_S anomalies

A number of factors affect seismic velocities, including temperature, partial melt, mineral composition and volatile content. We first attempt to identify and estimate effects caused by variations in composition. Some geodynamical models predict that melt extraction leaves behind a mantle residuum that is less dense but has higher seismic velocities than the ambient mantle (Jordan 1979; Phipps Morgan *et al.* 1995). A high-velocity anomaly was identified within the plume conduit in the asthenosphere beneath Iceland (Li & Detrick 2006) and in the lower lithosphere beneath the Galápagos Islands (Villagómez *et al.* 2007). For Iceland, eclogite melting and dehydration were proposed as possible mechanisms to increase the melting depth and ultimately seismic velocities of the residuum in the asthenosphere. Our images lack regions of anomalously high velocities in the lithosphere and the asthenosphere that can be associated with a melt residuum as predicted by Jordan (1979) and Phipps Morgan *et al.* (1995). This appears in puzzling contrast to studies in Iceland (Li & Detrick 2006) and the Galápagos Islands (Villagómez *et al.* 2007). There is a high-velocity anomaly to the east of Hawaii, but this location seems an unlikely location for anomalously high melt extraction.

Melt extraction need not result in increased seismic velocities, however. Under the Yellowstone hotspot, it has been suggested that melt extraction leaves behind a less dense mantle residuum, but seismic velocities may be reduced (by 0.5 per cent for V_P) or unchanged (for V_S) (Schutt & Lesher 2006). Seismic velocities in dry eclogite are about 5 per cent higher than in peridotite (Connolly & Kerrick 2002). For Hawaii, Hauri (1996) estimated the amount of eclogite in the upwelling mantle at 5 per cent by mass. A related velocity increase of no more than 0.3 per cent is probably on the order of our model errors. The melting and extraction of eclogite would lower seismic velocities in the mantle residuum. In our seismic model the strong low-velocity anomaly in the asthenosphere appears to branch toward the west and the south where many seamounts are located (Fig. 11). Because the seamounts are Cretaceous in age, however, the -1.5 per cent velocity anomaly in these branches is probably not related to recent thermal history. The lower velocities may therefore result from variations in composition, but it is not clear whether the seismic anomaly is principally the result of excess melt extraction.

To set a lower bound on a temperature anomaly associated with the peak-to-peak 6.2 per cent velocity-anomaly that we imaged in the asthenosphere to the west of Hawaii, we assume initially that 1.5 per cent is contributed by compositional variations, as just discussed. We then attribute the remaining anomaly (i.e. 4.7 per cent) to thermal effects (partial melt is discussed below). Wolfe *et al.* (2009) found that a purely thermal plume with a temperature anomaly of $\Delta T = 250$ °C is consistent with peak-to-peak shear velocity variations of 3 per cent imaged at 300 km depth. Anharmonic effects alone contribute with a temperature derivative $\partial(\ln V_S)/\partial T = -0.76 \times 10^{-4}\,\mathrm{K}^{-1}$ (Anderson & Isaak 1995). We use the formulation of Karato (1993) and Goes *et al.* (2000) to estimate the contributions from anelasticity. Global reference models represent the asthenosphere as a strongly attenuating, low-Q_μ zone, for example, the shear quality factor, Q_μ, is only 70 in model QL6 (Durek & Ekström 1996), compared with $Q_\mu = 191$ in the lithosphere above. A recent 3-D attenuation model appears to confirm this value beneath mid- to old-age ocean basins (Dalton *et al.* 2008). Given a geotherm for old oceanic mantle, we estimate the Q-adjusted temperature derivative to be $\partial(\ln V_S)/\partial T = -1.8 \times 10^{-4}\mathrm{K}^{-1}$, a value also derived from studies in North America (e.g. Godey *et al.* 2004) and for 20-Myr-old oceans at 150 km depth (Kreutzmann *et al.* 2004). A V_S anomaly of 4.7 per cent then results in a temperature anomaly of 260 °C, a value in good agreement with that obtained from PLUME body-wave tomography. There is evidence of reduced Q in a broad region around Hawaii (e.g. Gung & Romanowicz 2004; Dalton *et al.* 2008), but the reduction is likely less than 30 per cent. To obtain a realistic lower bound on the temperature anomaly, a lower $Q_\mu = 50$ would bring the temperature anomaly down to 215 °C, which approaches the value inferred from a magnetotelluric (MT) study that was conducted concurrently with the SWELL pilot study (Constable & Heinson 2004); see further discussion below.

Using our preferred derivative of $\partial(\ln V_S)/\partial T = -1.8 \times 10^{-4}\mathrm{K}^{-1}$, and assuming that the 6.2 per cent peak-to-peak velocity anomaly is purely thermal, we obtain $\Delta T = 350$ °C as an upper bound. The fact that the lithosphere is of nearly normal shear velocity directly above the pronounced low-velocity anomaly in the asthenosphere implies that much of the heat causing this anomaly may still be trapped below the lithosphere, as suggested by Li *et al.* (2004). On the other hand, in the lithosphere, Q_μ is likely larger, even around the Hawaiian hotspot, so that the same temperature anomalies cause smaller velocity anomalies: with $\partial(\ln V_S)/\partial T = -1.0 \times 10^{-4}\mathrm{K}^{-1}$ in the upper lithosphere (Kreutzmann *et al.* 2004), the 2.5 per cent-velocity anomaly found in the lithosphere would then correspond to a temperature anomaly of 250 °C. This ambiguity allows for the possibility that some of the heat has indeed already conducted into the upper lithosphere.

Partial melt causes a reduction in V_S, but its impact depends strongly on the geometry (e.g. the aspect ratio) of the embedded melt pockets. The partial derivative for $\ln V_S$ per 1 per cent melt fraction ranges between -0.8×10^{-2} and -8.5×10^{-2} at 50 km depth and between -0.6×10^{-2} and -7.1×10^{-2} at 200 km depth (Goes *et al.* 2000), depending on melt geometry (see also, Hammond & Humphreys 2000). For 20-Myr-old mantle beneath Iceland, Kreutzmann *et al.* (2004) inferred a value of -2.0×10^{-2}. Constable & Heinson (2004) found that a 100-km-wide plume conduit at 150 km depth, with a bulk melt fraction of likely 5–10 per cent, is required to fit their MT data collected across the SWELL pilot array, and a 200 °C temperature anomaly alone is inconsistent with their data. If the thermal anomaly is indeed around 250 °C, as suggested by body-wave tomography, and if we can assume that the 1.5 per cent anomaly initially attributed to compositional variations is actually due to partial melt near the conduit, then our shear velocity model can accommodate a partial melt fraction between 0.75 per cent, taking Kreutzmann *et al.* (2004) as a high estimate for the partial derivative, and 2 per cent, taking -0.7×10^{-2} as a low estimate for the partial derivative. If we assume that the smoothing constraints applied in our inversions can lead to an underestimation of V_S anomalies by as much as 1.0 per cent (see synthetic tests), then we could accommodate another 1.5 per cent of melt, for a total of 3.5 per cent. This amount would make the seismic model shown here marginally consistent with the results of the MT study. As noted above, a temperature anomaly of only 200 °C was assumed in the interpretation of the MT data, and a higher ΔT may require less melt to fit the MT observations as well.

It is tempting to associate a strong, 3.5 per cent low-velocity anomaly at depths less than 60 km in the north with the relatively young North Arch Volcanic Field and the Kauluakalana seamount (Fig. 14). A smaller anomaly to the southwest of Oahu seems to coincide with the Southwest Oahu Volcanic Field, and a larger anomaly southwest of Hawaii with the South Arch Volcanic Field. The North and South Arch Volcanic Fields contain widespread sheet flows. The seismic anomalies, some of which may reach into the asthenosphere, do not correlate well with the distribution of major seamounts in the area. Little is known of the crustal structure in these areas, but given our stringent frequency limits on the seismic data set we can assume that effects from variations in crustal structure are negligible. The seamounts, including Kauluakalana, are Cretaceous in age (H. Staudigel, personal communication, 2010; see also Sager 1987), and there should not be any remaining thermal signature (D. A. Clague, personal communication, 2009). The North Arch Volcanic Field, on the other hand, is extensive and formed more recently than 1.5 Myr ago (Frey *et al.* 2000; Clague *et al.* 2002), whereas the Southwest Oahu Volcanic Field, although also young (Hanyu *et al.* 2005), is smaller. The South Arch Volcanic Field is estimated to be younger than 20 000 years (Lipman *et al.* 1989). Because lava production in the North Arch Volcanic Field was widespread, the lithosphere was probably altered substantially, resulting in well-developed thermal and compositional signatures.

We also imaged a shallow, weak low-velocity anomaly to the far east of the island chain. Unfortunately the path coverage is low in this area, so the resolution is quite poor. However, several nearly parallel but crossing paths all trace anomalously low phase velocities at higher frequencies (Fig. 5), supportive of an anomaly confined to the lithosphere. We speculate that this anomaly is associated with narrow shear velocity anomalies along the Molokai and Maui Fracture Zones that are likely smeared out in our tomographic images. Complementary data are available from differential pressure gauges at one or two stations in this area, which may enhance the resolution of this feature.

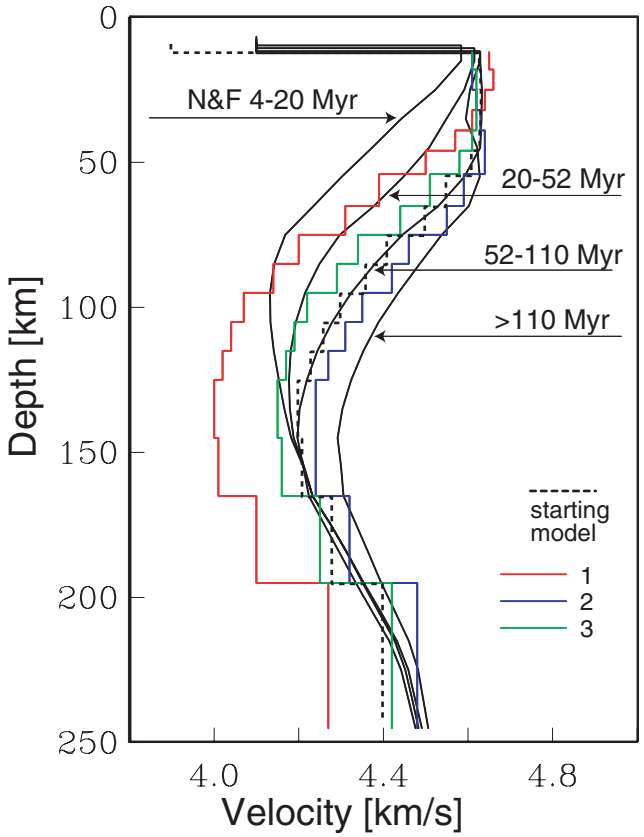

Figure 15. 1-D models of absolute shear velocity obtained at three locations marked by numbers in Fig. 11. Also shown are the models for age-dependent Pacific mantle by Nishimura & Forsyth (1989) as well as the starting model for this study.

7.3 Pacific plate rejuvenation

The existence and extent of lithosphere rejuvenation over the Hawaiian hotspot have long been debated, and our results provide important new constraints. Two processes have been suggested to contribute to lithosphere rejuvenation: (1) reheating of the lithosphere and (2) replacement of the lower lithosphere with asthenospheric material (Detrick & Crough 1978), a process also termed mechanical erosion (Li *et al.* 2004). Rejuvenation and thinning of the lithosphere are often used as synonyms though the degree of actual mechanical erosion is not known.

To assess the extent of lithosphere rejuvenation, we view the imaged mantle anomalies in the context of the strong vertical velocity gradients across the lithosphere and asthenosphere. Figs 15 and 16 show 1-D and 2-D absolute-velocity profiles through the V_S model of Fig. 11. The southwest–northeast (SW–NE) section emphasizes the asymmetry of the strong anomaly in the asthenosphere (100–180 km depth) about the axis of the island chain. Compared with 52–110-Myr-old oceanic mantle, velocities at location 1 within the strong low-velocity anomaly west of Hawaii (Fig. 11) are markedly reduced at depths greater than 75 km. In fact, velocities at depths greater than 100 km are even less than beneath young, 4–20-Myr-old oceanic lithosphere and approach some anomalously low velocities found beneath Iceland (Li & Detrick 2006), though the lowest velocities of about 4.0 km s^{-1} in our model are still higher than the lowest velocities found beneath Iceland (3.8–3.9 km s^{-1}). Rejuvenation of the lithosphere above this anomaly is also asymmetric, with 'thinner' than normal 100-Myr-old lithosphere found to the west of the islands. The 'thinning' of the lithosphere discussed here should be understood primarily as a velocity reduction in the lower lithosphere and not necessarily mechanical thinning, as it is difficult to define the lithosphere–asthenosphere boundary from a velocity model alone. Moderately anomalous velocity structure at on-swell location 3 is marked by slightly reduced velocities at depths between 75 and 170 km, whereas velocities at greater depths appear to return to normal values. By comparing bathymetry and the geoid with predictions from the seismic model, Laske *et al.* (2007) provided evidence that the lithosphere beneath the SWELL network experienced rejuvenation, but the approximately 100-km-thick lithosphere has likely not been mechanically eroded. Erosion may have occurred closer to the islands, northeast of the SWELL network, but meaningful estimates of the mechanical thickness of the lithosphere may require more detailed knowledge of the local attenuation structure than currently available. In their receiver function study, Li *et al.* (2000) did not find evidence of mechanical thinning beneath the island of Hawaii.

The low-velocity anomaly in the asthenosphere beneath the Hawaiian Swell appears to continue deeper. Our data lose resolution below the lower asthenosphere, and the anomalies may become larger in extent than shown here and continue deeper, as suggested by the PLUME body-wave studies (Wolfe *et al.* 2009, 2011). The northwest–southeast (NW–SE) cross-sections through our model

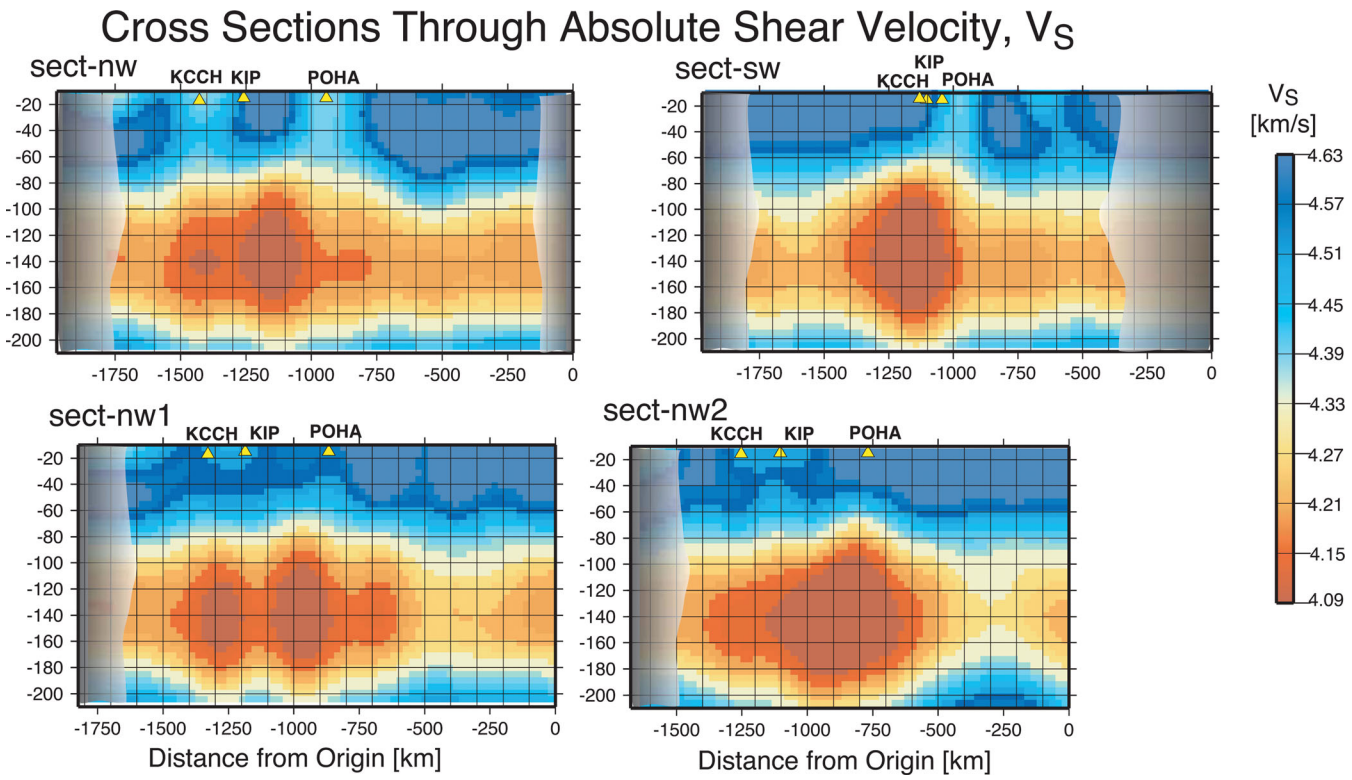

Figure 16. Cross-sections through the V_S model of Fig. 11, now displayed as absolute velocities. The locations of the sections are marked in Fig. 14. Structure near the ends of the profiles is poorly resolved and therefore has been shaded out. The projections of stations POHA, KIP and KCCH on the islands of Hawaii, Oahu and Kauai onto the sections are also marked (see Fig. 1).

(Fig. 16) show that the lithosphere has been altered downstream of the island of Hawaii, but the signal varies substantially across the swell, and a seismically near-normal lithosphere is found above the largest anomaly in the asthenosphere (section nw2 in Fig. 14). Li *et al.* (2004) argued for a thinning of the lithosphere from 100–110 km under the island of Hawaii to 50–60 km under Kauai, but our model indicates that the lower lithosphere beneath the island of Hawaii is itself affected by the underlying thermal anomaly. Li *et al.* (2004) speculated that a 're-aging' of the lithosphere could start beneath Kauai, but they lamented their lack of suitable data. Our model is consistent with such a process, if the V_S anomalies at 60 km depth are an indicator of such a recovery (Fig. 11), though our data coverage becomes poor far downstream from the islands. In their receiver function analysis, Li *et al.* (2004) found that the rise of the lithosphere–asthenosphere boundary is likely confined to within $\pm$150 km of the island chain, which is broadly consistent with our findings.

A narrow low-velocity feature in the lithosphere, no wider than 150 km, appears to connect to the surface near the islands and likely includes the pathways through which Hawaiian magmas reach the surface. As discussed above, the anomaly in the lithosphere to the far northeast of Hawaii may be associated with the Molokai and Maui Fracture Zones, but its extent is likely exaggerated as a result of poor path coverage.

An intriguing question remains whether rejuvenation of the lithosphere beneath the Hawaiian Swell is accompanied by a measurable heat flow signal. Early heat flow data collected along the swell margin from Hawaii to Midway (von Herzen *et al.* 1982) appeared to confirm the idea that a heat anomaly rejuvenates the lithosphere within 5 Myr, the time after which a significant heat flow anomaly can be observed at the surface. However, subsequent data from a profile crossing the seamount chain at about 170 $^\circ$ W were inconclusive (von Herzen *et al.* 1989), and it has been suggested that measurements in some areas with hydrothermal circulation are biased to lower values (Harris & McNutt 2007). For the along-swell heat flow profile of von Herzen *et al.* (1982), sites A, B and C shown in Fig. 14 exhibit no significant heat flow anomaly relative to that of a cooling oceanic plate. All remaining sites along that profile, which are outside our study area except for site E, returned significantly high heat flow anomalies. Site D was too close to the Molokai Fracture Zone to be reliably assessed. Sites A and C were located in areas of high seismic velocities in the asthenosphere, whereas B sits over a low-velocity anomaly. If we assume that the heat flow data at sites A, B and C are unaffected by hydrothermal circulation, and the low-velocity anomaly below site B is of thermal origin, then the fact that B shows normal heat flow suggests that heat associated with the seismic anomaly in the asthenosphere has not yet been conducted to the top of the lithosphere. The heat flow data do not correlate with our deep seismic anomaly, but there is good agreement with shallower structure. Sites A, B and C are located either within or near high-velocity anomalies at 40 km depth in the lithosphere, and only anomalous heat flow site E is located atop a low-velocity region that could carry a thermal anomaly. If the correspondence between shallow seismic anomalies and release of heat through the lithosphere holds, then cooling of the lithosphere may be uneven, and the collection of a heat flow data set that fully represents the first order along-axis cooling of the Pacific Plate may be a complex task. It would be of interest to know the seismic structure beneath the other heat flow measurement sites downstream. Unfortunately, no regional data sets are available, and global data sets have yet to attain the resolution needed to ascertain even the sign of anomalies in this area. Embedding the PLUME data set in a global tomographic

inversion or a follow-up OBS experiment halfway between Kauai and Midway could help resolve this open question.

8 SUMMARY AND CONCLUDING REMARKS

The most robust feature imaged by Rayleigh-wave phase velocity tomography is a pronounced low-velocity anomaly in the asthenosphere that is centred to the west of the island of Hawaii. The most anomalous area is quite narrow, 100 km in east–west extent and 200 km in its long direction (Figs 14 and 16). Because path coverage is best near the island of Hawaii, it is rather unlikely that this anomaly extends beneath the island. At depths shallower than ∼60 km, a low-velocity anomaly is strongest between the islands of Hawaii and Maui. With an alternative inversion approach, this anomaly is spread over a 200-km-wide region centred on Hawaii. We interpret these anomalies as the signature of the thermal rejuvenation of the Pacific lithosphere. Rejuvenation can occur in the form of upward migration of heat and melt as a result of either fracturing of the plate or transport from the top of an underlying hot mantle plume. Evidence from PLUME body-wave tomography (Wolfe *et al.* 2009, 2011) lends support for the latter interpretation. The excess temperature in the asthenosphere is likely between 200 and 250 °C, and the degree of partial melting may be as high as several percent but likely no more than 3.5 per cent.

In this study, we have used ray theory, and it will be important to test the robustness of our model using other approaches such as finite-frequency theory (Zhou *et al.* 2006). We expect that the general locations of anomalies are robust, but their amplitudes may increase somewhat, because ray theory does not account for wavefront healing effects after passage through small anomalous regions. Finite-frequency modelling has found its way into regional surface wave analyses (e.g. Villagómez *et al.* 2007; Chevrot & Zhao 2007; Chen *et al.* 2007) though others still use the ray approach (Li & Detrick 2006). There is still considerable debate over which finite-frequency approach (e.g. 2-D, fat-ray, single-Born scattering or full 3-D kernels) yields the best model to describe true structure. Finite-frequency theory also introduces a dependence on the seismic source, and its uncertainties, adding a layer of complexity. Depending on how the kernels are averaged over frequency, discrepancies between models resulting from different finite-frequency approaches may reach the same magnitude as those between these and a model obtained with ray theory. Also, to more accurately assess the causes of the velocity anomalies found here, we will likely need accurate images of attenuation, as higher attenuation increases the sensitivity of seismic velocities to variations in temperature. It may turn out that the benefits of using finite-frequency theory instead of ray theory are offset by properly taking into account effects of attenuation on the velocities–temperature scaling, and ignoring both, as we have done here, may leave the interpretation little affected. At the very least, the model presented here serves as benchmark.

Because azimuthal anisotropy in the region varies and its magnitude can be as much as 5 per cent (Laske *et al.* 2007; Chojnacki *et al.* 2009), a study of how anisotropy affects the imaged distribution of the isotropic velocities is also warranted. It is premature to quantify the effects from ignoring azimuthal anisotropy around Hawaii, but we should stress that many of the cells in our maps are illuminated from a wide range of azimuths. Of all oceanic regions worldwide, the area surrounding Hawaii is probably the region with the best azimuthal coverage of large teleseismic events, and misestimation of shear velocity anomalies should probably amount to no more than 0.5 per cent. The horizontal seismometer components were often sufficiently quiet to allow the measurement of Love wave dispersion. Incorporating such data into the inversions will further help to constrain mantle-flow patterns beneath and around the Hawaiian Swell.

ACKNOWLEDGMENTS

We thank the WHOI and SIO OBSIP teams as well as the CIW network team for their tireless efforts to build, deploy and recover the instruments used in this experiment and to provide the data in a user-friendly format. We thank the officers and crews of R/Vs Melville, Ka'imikai-o-Kanaloa and Kilo Moana for four well-executed cruises, and Beecher Wooding and the JASON team for successfully rescuing two instruments at sites crucial for data coverage. The operators of GEOSCOPE, GSN, and GEOFON as well as IRIS and its Data Management Center provided data from the observatory stations and the PLUME land stations. We also thank David Clague and Jerry Winterer for stimulating discussions. We thank two anonymous reviewers for comments that helped improve the manuscript. Spencer Trinh helped with data processing. This research was financed by the National Science Foundation under grants OCE-00-02470 and OCE-00-02819. Markee was partly sponsored by a SIO graduate student fellowship.

REFERENCES

Anderson, O.L. & Isaak, D.G., 1995. Elastic constants of mantle minerals at high temperature, in *Mineral Physics and Crystallography, A Handbook of Physical Constants,* pp. 64–97, ed. Ahrens, T.J., American Geophysical Union, Washington, D.C.

Backus, G. & Gilbert, F., 1968. The resolving power of gross Earth data, *Geophys. J. R. astron. Soc.,* **16,** 169–205.

Chen, P., Zhao, L. & Jordan, T.H., 2007. Full 3D seismic waveform tomography for the Los Angeles Basin area, *Bull. seism. Soc. Am.,* **97,** 1094–1120.

Chevrot, S. & Zhao, L., 2007. Multiscale finite-frequency Rayleigh wave tomography of the Kaapvaal craton, *Geophys. J. Int.,* **169,** 201–215.

Chojnacki, P. *et al.*, 2009. Rayleigh wave azimuthal anisotropy observed during the Hawaiian PLUME project, *EOS, Trans. Am. geophys. Un.,* **90**(52), Fall Meet. Suppl., Abstract S11A-1687.

Clague, D.A., Uto, K., Satake, K. & Davis, A.S., 2002. Eruption style and flow emplacement in the submarine North Arch Volcanic Field, Hawaii, in *Hawaiian Volcanoes: Deep Underwater Perspectives,* pp. 65–84, eds Takahashi, E., Lipman, P.W., Garcia, M.O., Naka, J. & Aramaki, S., Geophys. Monograph Series 128, American Geophysical Union, Washington, D.C.

Collins, J.A., Vernon, F.L., Orcutt, J.A. & Stephen, R.A., 2002. Upper mantle structure beneath the Hawaiian swell: constraints from the ocean seismic network pilot experiment, *Geophys. Res. Lett.,* **29,** 1522, doi:10.1029/2001GL013302.

Connolly, J.A.D. & Kerrick, D.M., 2002. Metamorphic controls on seismic velocity of subducted oceanic crust at 100–250 km depth, *Earth planet. Sci. Lett.,* **204,** 61–74.

Constable, S. & Heinson, G., 2004. Hawaiian hot-spot swell structure from seafloor MT sounding, *Tectonophysics,* **389,** 111–124, doi:10.1016/j.tecto.2004.07.060.

Constable, S.C., Parker, R.L. & Constable, C.G., 1987. Occam's inversion: a practical algorithm for generating smooth models from electromagnetic sounding data, *Geophysics,* **52,** 289–300.

Cox, C., Deaton, T. & Webb, S., 1984. A deep-sea differential pressure gauge, *J. Atmos. Oceanic Technol.,* **1,** 237–346.

Dalton, C.A., Ekström, G. & Dziewonski, A.M., 2008. The global attenuation structure of the upper mantle, *J. geophys. Res.,* **113,** B09303, doi:10.1029/2007JB005429.

Davies, G.F., 1988. Ocean bathymetry and mantle convection. 1. Large-scale flow and hotspots, *J. geophys. Res.,* **93,** 10 467–10 480.

Detrick, R.S. & Crough, S.T., 1978. Island subsidence, hot spots, and lithospheric thinning, *J. geophys. Res.,* **83,** 1236–1244.

Durek, J.J. & Ekström, G., 1996. A radial model of anelasticity consistent with long-period surface-wave attenuation, *Bull. seism. Soc. Am.,* **86,** 144–158.

Efron, B., 1987. *The Jackknife, the Bootstrap, and Other Resampling Plans,* p. 92, Society for Industrial and Applied Mathematics, Philadelphia, PA.

Frey, F.A., Clague, D.A., Mahoney, J. & Sinton, J., 2000. Volcanism at the edge of the Hawaiian plume: petrogenesis of submarine alkalic lavas from the North Arch Volcanic Field, *J. Petrol.,* **41,** 667–691.

Godey, S., Deschamps, F. & Trampert, J., 2004. Thermal and compositional anomalies beneath the North American continent, *J. geophys. Res.,* **109,** B01308, doi:10.1029/2002JB002263.

Goes, S., Govers, R. & Vacher, P., 2000. Shallow mantle temperatures under Europe from *P* and *S* wave tomography, *J. geophys. Res.,* **105,** 11 153–11 169.

Gung, Y. & Romanowicz, B., 2004. *Q* tomography of the upper mantle using three-component long-period waveforms, *Geophys. J. Int.,* **157,** 813–830.

Hammond, W.C. & Humphreys, E.D., 2000. Upper mantle seismic wave velocity: effects of realistic partial melt geometries, *J. geophys. Res.,* **105,** 10 975–10 986.

Hanyu, T., Clague, D.A., Kaneoka, I., Dunai, T.J. & Davies, G.R., 2005. Noble gas study of on- and off-axis alkali volcanism at the Hawaiian hotspot, *Chem. Geol.,* **214,** 135–155.

Harris, R.N. & McNutt, M.K., 2007. Heat flow on hot spot swells: evidence for fluid flow, *J. geophys. Res.,* **112,** B03407, doi:10.1029/2006JB004299.

Hauri, E.H., 1996. Major-element variability in the Hawaiian mantle plume, *Nature,* **382,** 415–419.

von Herzen, R.P., Detrick, R.S., Crough, S.T., Epp, D. & Fehn, U., 1982. Thermal origin of the Hawaiian Swell: heat flow evidence and thermal models, *J. geophys. Res.,* **87,** 6711–6723.

von Herzen, R.P., Cordery, M.J., Detrick, R.S. & Fang, C., 1989. Heat flow and the thermal origin of hot spot swells: the Hawaiian Swell revisited, *J. geophys. Res.,* **94,** 13 783–13 799.

Jordan, T.H., 1979. Mineralogies, densities, and seismic velocities of garnet lherzolites and their geophysical implications, in *The Mantle Sample: Inclusions in Kimberlites and Other Volcanics,* Vol 2., pp. 1–14, eds Boyd, F.R. & Meyer, H.O.A., American Geophysical Union, Washington, D.C.

Karato, S., 1993. Importance of anelasticity in the interpretation of seismic tomography, *Geophys. Res. Lett.,* **20,** 1623–1626.

Katzman, R., Zhao, L. & Jordan, T.H., 1998. High-resolution, two-dimensional vertical tomography of the central Pacific mantle using *ScS* reverberations and frequency-dependent travel times, *J. geophys. Res.,* **103,** 17 933–17 971.

Kreutzmann, A., Schmeling, H., Junge, A., Ruedas, T., Marquart, G. & Bjarnason, I. Th., 2004. Temperature and melting of a ridge-centered plume with applications to Iceland. Part II: predictions for electromagnetic and seismic observables, *Geophys. J. Int.,* **159,** 1097–1111.

Laske, G. & Masters, G., 1996. Constraints on global phase velocity maps from long-period polarization data, *J. geophys. Res.,* **101,** 16 059–16 075.

Laske, G., Phipps Morgan, J. & Orcutt, J.A., 1999. First results from the Hawaiian SWELL pilot experiment, *Geophys. Res. Lett.,* **26,** 3397–3400, doi:10.1029/1999GL005401.

Laske, G., Phipps Morgan, J. & Orcutt, J.A., 2007. The Hawaiian SWELL pilot experiment: evidence for lithosphere rejuvenation from ocean bottom surface wave data, in *Plates, Plumes and Planetary Processes,* Special Paper 430, pp. 209–233, eds Foulger, G.R. & Jurdy, D.M., Geological Society of America, Boulder, CO.

Laske, G., Collins, J.A., Wolfe, C.J., Solomon, S.C., Detrick, R.S., Orcutt, J.A., Bercovici, D. & Hauri, E.H., 2009a. Probing the Hawaiian hot spot with new broadband ocean bottom instruments, *EOS, Trans. Am. geophys. Un.,* **90,** 362–363.

Laske, G. *et al.*, 2009b. Surface waves from the Hawaiian PLUME project trace anomalously slow lithosphere and asthenosphere, *Geophys. Res. Abstr.,* **11,** EGU2009-6525.

Li, A. & Detrick, R.S., 2006. Seismic structure of Iceland from Rayleigh wave inversions and geodynamic implications, *Earth planet. Sci. Lett.,* **241,** 901–912.

Li, X., Kind, R., Priestley, K., Sobolev, S.V., Tilmann, F., Yuan, X. & Weber, M., 2000. Mapping the Hawaiian plume with converted seismic waves, *Nature,* **405,** 938–941.

Li, X., Kind, R., Yuan, X., Wölbern, I. & Hanka, W., 2004. Rejuvenation of the lithosphere by the Hawaiian plume, *Nature,* **427,** 827–829.

Lipman, P.W., Clague, D.A., Holcomb, R.T. & Moore, J.G., 1989. Newly identified young lava flows on the sea floor south of the Hawaiian Ridge, *Geology,* **7,** 611–614.

Markee, A. *et al.*, 2008. Surface wave tomography for the Hawaiian PLUME project and the seismic structure of the Hawaiian Swell, *EOS, Trans. Am. geophys. Un.,* **89**(53), Fall Meet. Suppl., Abstract DI21A-1723.

Maupin, V., 1992. Modelling of laterally trapped surface waves with application to Rayleigh waves in the Hawaiian swell, *Geophys. J. Int.,* **110,** 553–570.

Morgan, W.J., 1971. Convection plumes in the lower mantle, *Nature,* **230,** 42–43.

Müller, R.D., Sdrolias, M., Gaina, C. & Roest, W.R., 2008. Age, spreading rates and spreading symmetry of the world's ocean crust, *Geochem. Geophys. Geosyst.,* **9,** Q04006, doi:10.1029/2007GC001743.

Natland, J.H. & Winterer, E.L., 2005. Fissure control on volcanic action in the Pacific, in *Plumes, Plates and Paradigms,* Special Paper 388, pp. 687–710, eds Foulger, G.R., Natland, J.H., Presnall, D.C. & Anderson, D.L., Geological Society of America, Boulder, Colorado.

Nishimura, C.E. & Forsyth, D.W., 1989. The anisotropic structure of the upper mantle in the Pacific, *Geophys. J. Int.,* **96,** 203–229.

Nolet, G., 1990. Partitioned waveform inversion and two-dimensional structure under the network of autonomously recording seismographs, *J. geophys. Res.,* **95,** 8499–8512.

Olson, P., 1990. Hot spots, swells, and mantle plumes, in *Magma Transport and Storage,* pp. 33–51, ed. Ryan, M.P., John Wiley, New York, NY.

Phipps Morgan, J., Morgan, W.J. & Price, E., 1995. Hotspot melting generated both hotspot volcanism and a hotspot swell? *J. geophys. Res.,* **100,** 8045–8062.

Priestley, K. & Tilmann, F., 1999, Shear-wave structure of the lithosphere above the Hawaiian hot spot from two-station Rayleigh wave phase velocity measurements, *Geophys. Res. Lett.,* **26,** 1493–1496.

Ribe, N.M. & Christensen, U.R., 1999. The dynamical origin of Hawaiian volcanism, *Earth planet. Sci. Lett.,* **171,** 517–531.

Sager, W.W., 1987. Late Eocene and Maastrichtian paleomagnetic poles for the Pacific plate: implications for the validity of seamount paleomagnetic data, *Tectonophysics,* **144,** 301–314.

Schutt, D.L. & Lesher, C.E., 2006. Effects of melt depletion on the density and seismic velocity of garnet and spinel lherzolite, *J. geophys. Res.,* **111,** B05401, doi:10.1029/2003JB002950.

Sleep, N.H., 1990. Hotspots and mantle plumes: some phenomenology, *J. geophys. Res.,* **95,** 6715–6736.

Slepian, D., 1978. Prolate spheroidal wave functions, Fourier analysis, and uncertainty. V: the discrete case, *Bell. Syst. Tech. J.,* **57,** 1371–1430.

Strader, A.E. *et al.*, 2009. Rayleigh-wave group velocity tomography in the vicinity of the Hawaiian hotspot, *EOS, Trans. Am. geophys. Un.,* **90**(53), Fall Meet. Suppl., Abstract S53A-1476.

Thomson, D.J., 1982. Spectrum estimation and harmonic analysis, *Proc. IEEE,* **70,** 1055–1096.

Tilmann, F.J., Benz, H.M., Priestley, K.F. & Okubo, P.G., 2001. *P*-wave velocity structure of the uppermost mantle beneath Hawaii from traveltime tomography, *Geophys. J. Int.,* **146,** 594–606.

Turcotte, D.L. & Oxburgh, E.R., 1973. Mid-plate tectonics, *Nature,* **244,** 337–399.

Van Ark, E. & Lin, J., 2004. Time variation in igneous volume flux of the Hawaiian-Emperor hotspot seamount chain, *J. geophys. Res.,* **109,** B11401, doi:10.1029/2003JB002949.

Villagómez, D.R., Toomey, D.R., Hooft, E.E.E. & Solomon, S.C., 2007. Upper mantle structure beneath the Galápagos Archipelago from surface wave tomography, *J. geophys. Res.,* **112,** B07303, doi:10.1029/2006JB004672.

Watts, A.B., 1976, Gravity and bathmetry in the central Pacific Ocean, *J. geophys. Res.,* **81,** 1533–1553.

Webb, S.C., 1998, Broadband seismology and noise under the ocean, *Rev. Geophys.,* **36,** 105–142.

Wessel, P., 1993. Observational constraints on models of the Hawaiian hot spot swell, *J. geophys. Res.,* **98,** 16 095–16 104.

Wilson, J.T., 1963. A possible origin of the Hawaiian Islands, *Can. J. Phys.,* **41,** 863–868.

Wölbern, I., Jacob, A.W.B., Blake, T.A., Kind, R., Li, X., Yuan, X., Duennebier, F. & Weber, M., 2006. Deep origin of the Hawaiian tilted plume conduit derived from receiver functions, *Geophys. J. Int.,* **166,** 767–781.

Wolfe, C.J., Solomon, S.C., Silver, P.G., vanDecar, J.C. & Russo, R.M., 2002. Inversion of body-wave delay times for mantle structure beneath the Hawaiian Islands: results from the PELENET experiment, *Earth planet. Sci. Lett.,* **198,** 129–145, doi:10.1016/S0012-821X(02)00493-4.

Wolfe, C.J., Solomon, S.C., Laske, G., Collins, J.A., Detrick, R.S., Orcutt, J.A., Bercovici, D. & Hauri, E.H., 2009. Mantle shear-wave velocity structure beneath the Hawaiian hot spot, *Science,* **326,** 1388–1390, doi:10.1126/science.1180165.

Wolfe, C.J., Solomon, S.C., Laske, G., Collins, J.A., Detrick, R.S., Orcutt, J.A., Bercovici, D. & Hauri, E.H., 2011. Mantle *P*-wave velocity structure beneath the Hawaiian hot spot, *Earth planet. Sci. Lett.,* **303,** 267–280.

Woods, M.T., Leveque, J.-J., Okal, E.A. & Cara, M., 1991. Two-station measurements of Rayleigh wave group velocity along the Hawaiian Swell, *Geophys. Res. Lett.,* **18,** 105–108.

Woods, M.T. & Okal, E.A., 1996. Rayleigh-wave dispersion along the Hawaiian Swell: a test of lithospheric thinning by thermal rejuvenation at a hotspot, *Geophys. J. Int.,* **125,** 325–339.

Zhou, Y., Nolet, G., Dahlen, F.A. & Laske, G., 2006. Global upper-mantle structure from finite-frequency surface-wave tomography, *J. geophys. Res.,* **111,** doi:10.1029/2005JB003677.

SUPPORTING INFORMATION

Additional Supporting Information may be found in the online version of this article:

Appendix A. Additional material on phase velocity data.
Appendix B. Approach A—three-dimensional shear velocity from path-averaged 1-D models.

Please note: Wiley-Blackwell are not responsible for the content or functionality of any supporting materials supplied by the authors. Any queries (other than missing material) should be directed to the corresponding author for the article.

GJI-11-0015

Online supplement to: Asymmetric Shallow Mantle Structure beneath the Hawaiian Swell – Evidence from Rayleigh Waves Recorded by the PLUME Network

Gabi Laske[1], Amanda Markee[1], John A. Orcutt[1], Cecily J. Wolfe[3], John A. Collins[2], Sean C. Solomon[4], Robert S. Detrick[2], David Bercovici[5] and Erik H. Hauri[4]

[1] *Institute of Geophysics and Planetary Physics, University of California San Diego, CA 92093-0225, USA.*

Email: glaske@ucsd.edu

[2]*Department of Geology and Geophysics, Woods Hole Oceanographic Institution, Woods Hole, MA 02543, USA*

[3] *Hawaii Institute of Geophysics and Planetology, University of Hawaii at Manoa, Honolulu, HI 96822, USA*

[4]*Department of Terrestrial Magnetism, Carnegie Institution of Washington, Washington, DC 20015, USA*

[5]*Department of Geology and Geophysics, Yale University, New Haven, CT 06520, USA*

APPENDIX A: ADDITIONAL MATERIAL ON PHASE VELOCITY DATA

For each two-station path, a particular earthquake was considered only if its source azimuth was no more than 10° from the two-station great-circle azimuth. The number of suitable events varied greatly among two-station paths. Of the 614 paths analyzed, 124 paths were constrained by only up to five events each, but more than half of the paths (358) were constrained by more than 10 events (Fig. A1). For each path, the final path-averaged phase velocity curve was then given by the weighted average over all suitable events, and the final errors were typically ten times smaller than those of single-event data. Figs. 5 and 6 show the path-averaged phase velocities and their uncertainties along each of the 614 paths at four frequencies.

A summary of the misfit, χ^2/N, of the V_S model to the phase velocity maps is given in map view in Fig. A2. The misfit was calculated for each of the 13×13 one-degree cells in the map, and the "data" to be fit were the 81 phase velocity values between 10 and 50 mHz. For misfits $\chi^2/N = 1$ the model fits the data.

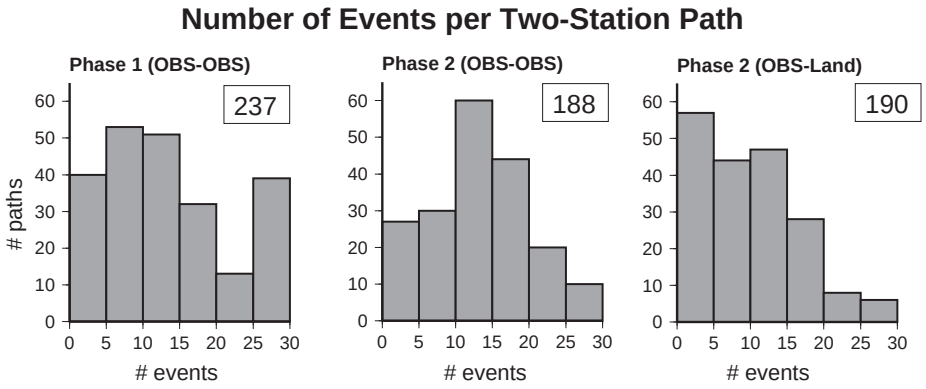

Figure A1. Event statistics for all two-station paths used in this study. The histograms show the number of dispersion curves that are constrained by a given number of events. A higher number of events typically leads to more precise dispersion curves. Histograms are shown for different groups in the dataset: 237 paths for the phase-1 deployment, 188 paths for the phase-2 deployment that involve only OBS sites, and 190 paths from phase 2 that involve one OBS and one land site. No paths involving only land sites were included in this analysis.

For $\chi^2 < 1$ the model overfits the data, which is the case in most of the cells, except for two locations. The misfit is relatively large near station PL38 on the western edge of the maps, where data coverage is relatively poor (see the path coverage map in Fig. 9). Because of early failure, PL38 did not produce many reliable constraints. The large misfit found north of Maui, where data coverage is good, suggests that the data there are slightly internally inconsistent.

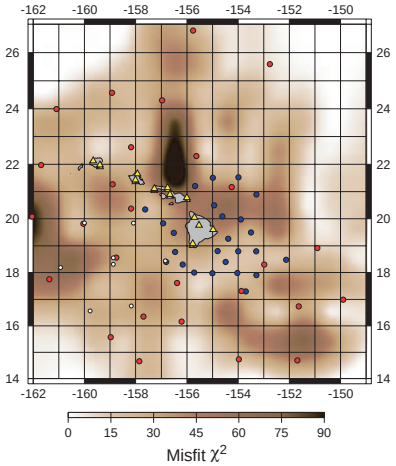

Figure A2. Misfit map displaying the ability of the V_S model of Fig. 10 to fit the phase velocity maps of Fig. 7. The data misfit trades off with the model roughness, whereby a laterally rougher model provides a better overall fit to the phase velocity data for most of the 13×13 one-degree cells. For some cells, the fit to the data may change very slowly when a different model is chosen along the trade-off curve between roughness and misfit.

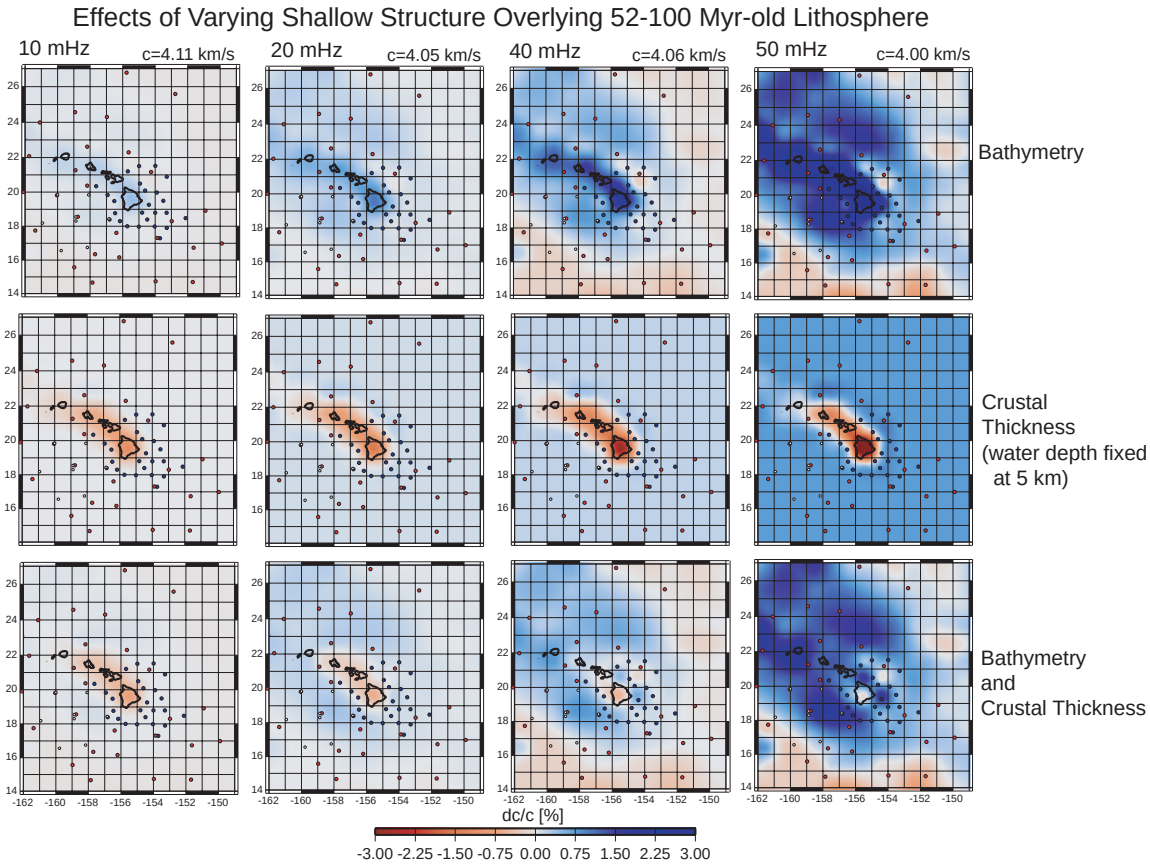

Figure A3. Predictions of phase velocity anomaly resulting from variations in bathymetry and crustal thickness at four frequencies between 10 and 50 mHz. Top row: effects from variations only in bathymetry. Middle row: effects from variations only in crustal thickness for a fixed seafloor depth of 5 km. Bottom row: effects from the combined variation of both. Because of their opposite effects, signals from bathymetry and crustal thickness variations partially cancel one another, except at the highest frequencies. The maps show percentage perturbations to a frequency-dependent reference velocity, which is given in the upper right corner of each column of maps. Crustal thickness was estimated to be 20 km beneath the island of Hawaii and up to 15 km beneath the other islands. Oceanic crust was assumed to be 6.5 km thick. Island and oceanic crustal thickness were weighted in each $1^\circ \times 1^\circ$ cell by their fractional area. The contribution from seamounts was not considered, as little is known about their crustal structure.

Lateral variations in bathymetry and crustal structure affect variations in local phase velocity, particularly at higher frequencies. For the frequencies considered, these effects are relatively minor, except near 50 mHz (Fig. A3). To estimate the effects caused by variations in bathymetry and crustal structure on the final V_S model, we repeated our inversion using local phase velocity maps that were corrected for these effects (Fig. A4). A model resulting from inverting phase data up to only 40 mHz to further reduce sensitivity to crustal structure is shown in Fig. A5. The resulting models are nearly identical to the model shown in Fig. 10.

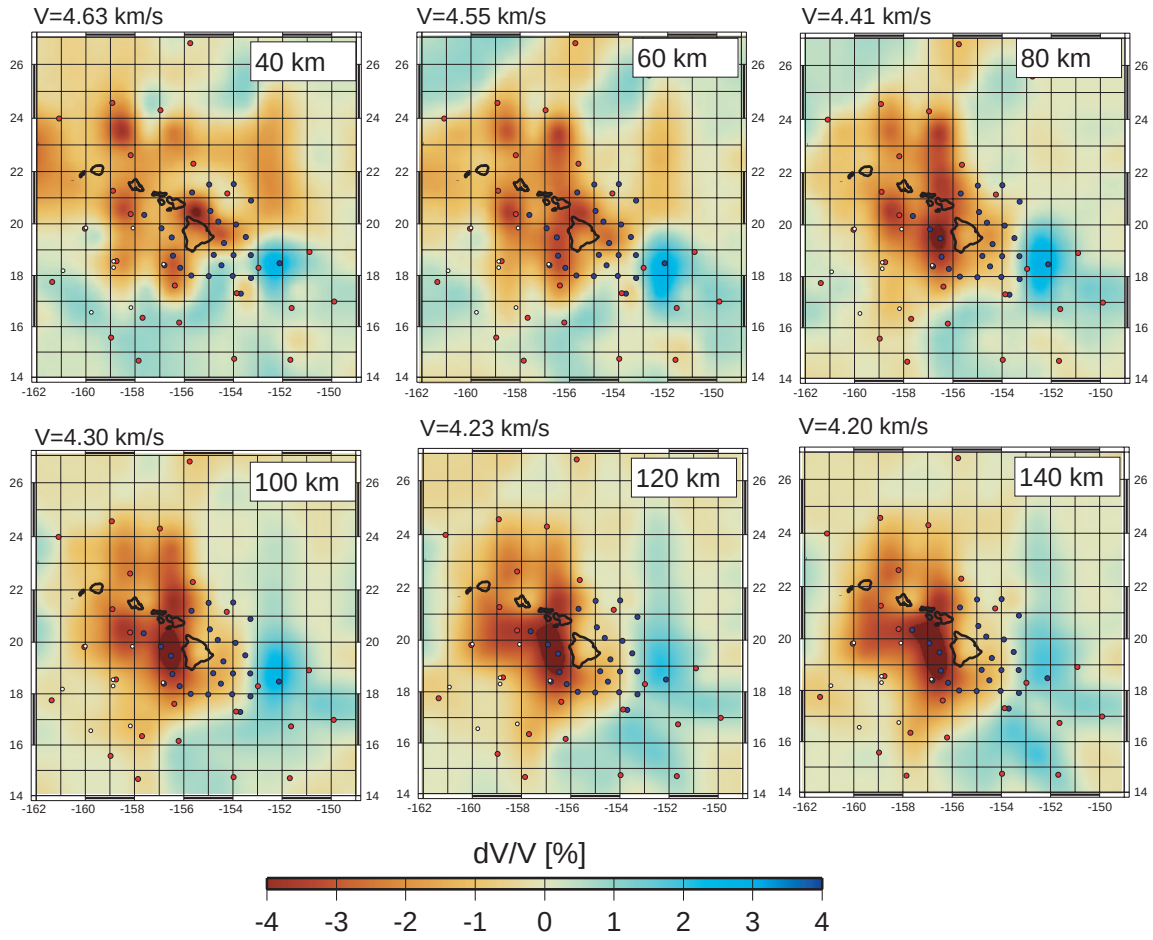

Figure A4. Model of shear velocity anomaly, dV_S/V_S, after the phase velocity maps were corrected for effects caused by bathymetry and crustal thickness (Fig. A3). For clarity in the panels, the subscript is omitted. The six panels show percentage perturbations to the reference model at depths between 40 and 140 km. The reference model is the modified N&F model for 52–100-Myr-old lithosphere. The reference velocity at each depth is given above each panel. Different symbols mark the PLUME phase 1 (blue) and phase 2 (red) OBS sites, as well as those of the SWELL pilot experiment (white).

Synthetic tests when only the PLUME data are included in the inversions are shown in Figs. A6 and A7. Recovery in the area covered by the SWELL pilot array is somewhat reduced compared to tests when the SWELL data are included (Figs. 12 and 13).

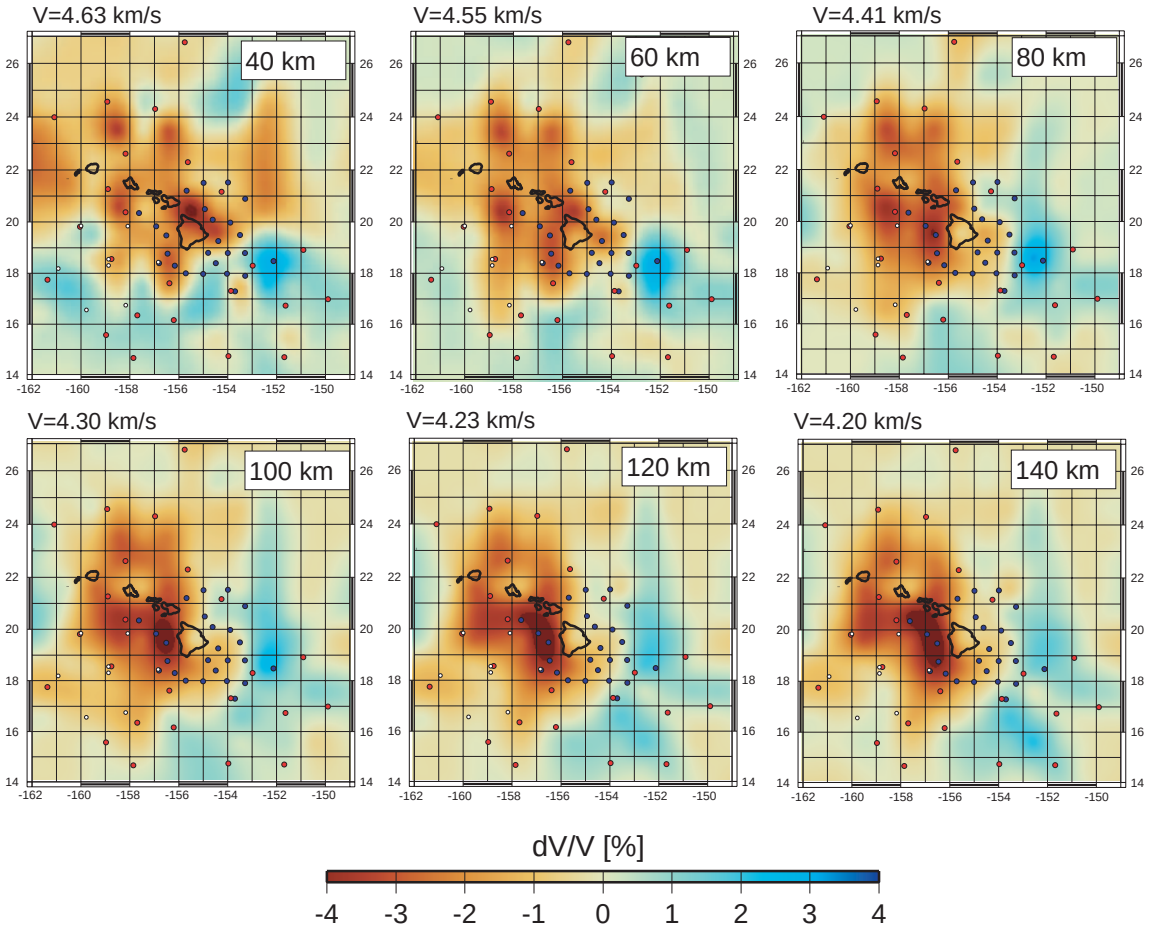

Figure A5. Same as Fig. A4, but using data only between 10 and 40 mHz. Sensitivity of the modeling to bathymetry and crustal structure is reduced over this frequency band. See Fig. A4 for details.

APPENDIX B: APPROACH A – THREE-DIMENSIONAL SHEAR VELOCITY FROM PATH-AVERAGED 1-D MODELS

This section describes the parameterization and inversions for approach A. We used the same methodology as for approach B, with the main difference that the inversions for vertical and lateral structure are switched.

Surface waves are sensitive to shear velocity, V_S, as well as compressional velocity, V_P, and density, ρ, but the most dominant and best-resolved parameter is V_S (see online supplement of Laske *et al.* 2007). To limit the number of model parameters for a well-conditioned inverse problem, tomographers often ignore sensitivity to V_P and ρ. Such a strategy could lead to biased models where, e.g., shallow V_P structure can be mapped into deeper V_S structure. We prefer to scale the kernels for V_P, $\tilde{K}_P$, and ρ, $\tilde{K}_R$, and include them in a single kernel for V_S, $\tilde{K}_S$, using the following scaling:

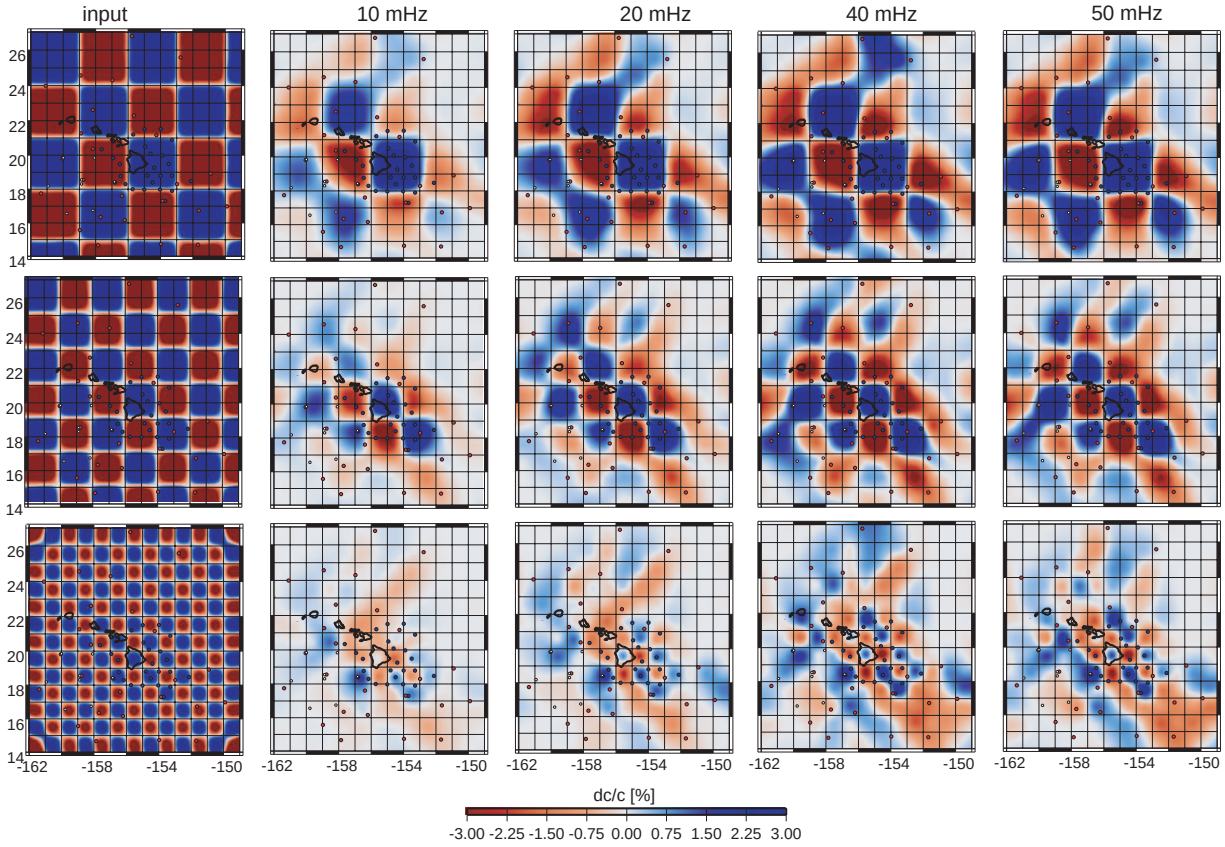

Figure A6. Checkerboard recovery tests for three input models with input squares of varying size (left column). These tests include the PLUME data only. The magnitude of the input anomaly is $\pm 5\%$. The size of the squares in the model on the bottom is 1°, which is the grid size in the parameterization.

$$\begin{aligned} \tilde{K}_P \cdot \delta V_P &= (1/1.7)\tilde{K}_S \cdot \delta V_S \\ \tilde{K}_R \cdot \delta \rho &= (1/2.5)\tilde{K}_S \cdot \delta V_S \end{aligned} \tag{B.1}$$

The scaling factors come from both theoretical and experimental studies (e.g., Anderson *et al.* 1968; Anderson & Isaak 1995) under the conditions of high temperatures and low pressures found in the upper mantle as well as from globally observed $SS - S$ and $PP - P$ differential travel-time data (Masters et al. 2000). These factors are applicable as long as strong compositional changes or large quantities of partial melt (e.g., $> 10\%$) are not present.

As a starting model, we used a modified Nishimura & Forsyth (1989) model (N&F) for 52–110-Myr-old lithosphere (Laske *et al.* 2007). The crustal layer was adjusted to reflect results from seismic sounding experiments in the surrounding ocean (for details see Laske *et al.* 2007). The model was parameterized in 17 layers of constant velocity; the layer thickness is 7 km near the top and increases with depth, acknowledging the degrading resolution with depth (Fig. 3). Because the 10 mHz data are sensitive to structure deeper than

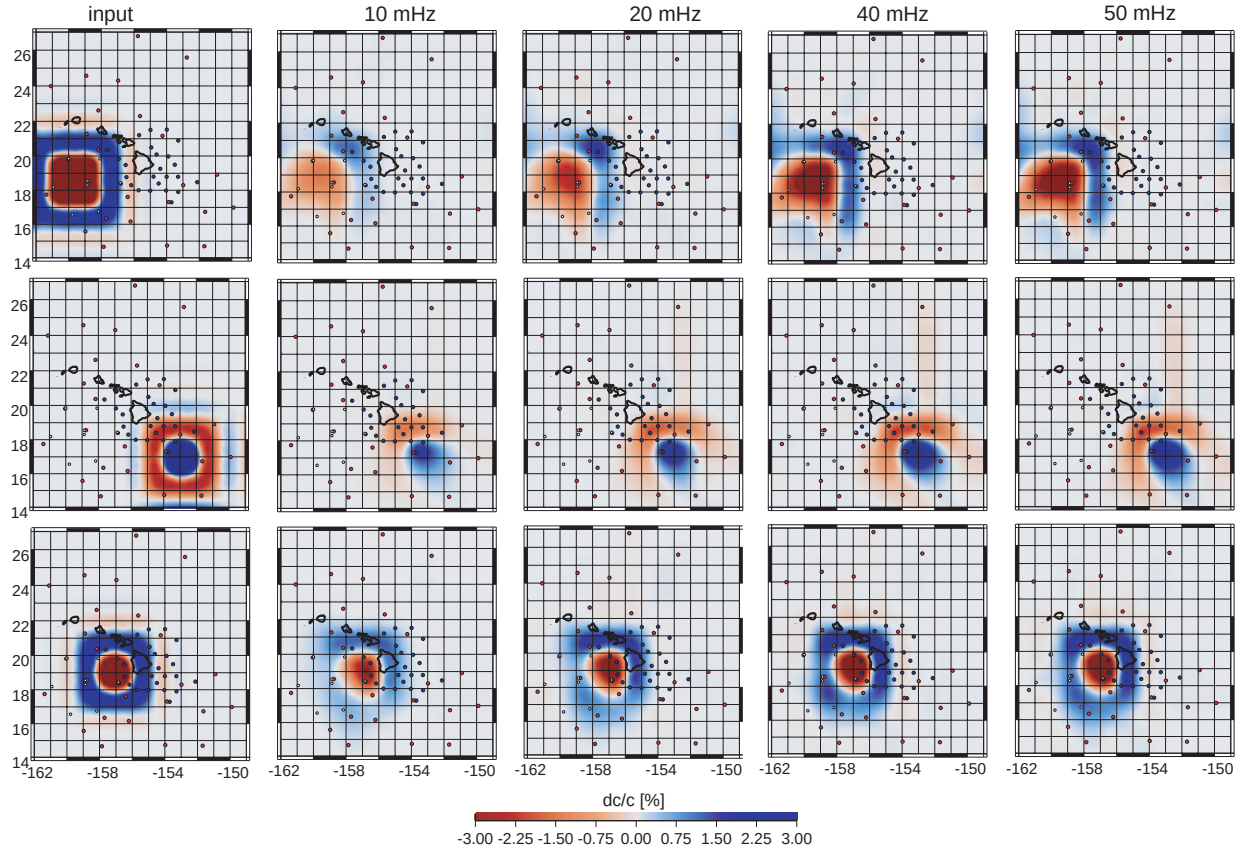

Figure A7. Recovery tests for isolated input anomalies at three different locations for four frequencies. These tests include the PLUME data only. See Fig. A7 for details.

200 km, the bottom layer in the model is 50 km thick and ends at 245 km depth. Velocities retrieved at these depths are uncertain, and we do not interpret them, but including such a layer in the inversion avoids artificial mapping of deep structure into shallower layers. The two top layers at depths less than 20 km are also excluded from interpretation. These two layers are intended to absorb unmodelled variations in bathymetry and crustal structure. By inspecting Fig. A3, we verify that effects from bathymetry and crustal structure are nearly negligible except at frequencies of 50 mHz and above.

In an Occam's smoothed inversion (Constable *et al.* 1987), we seek vertically smooth perturbations to the starting model that fit our data to within an acceptable misfit, χ^2/N, where $\chi = x_d - x_t$, x_d is the datum, x_t the prediction, and N the number of data. Formally, we seek to minimize the misfit function, M.F., which is the weighted sum of data prediction error, χ^2, or the misfit, and model roughness, $\partial\mathbf{m}$

$$\text{M.F.} = \chi^2 + \mu \left| \mathbf{m^T} \partial^{\mathbf{T}} \partial \mathbf{m} \right| \tag{B.2}$$

where $\mathbf{m}$ is the model vector, μ the smoothing or regularization parameter, and ^{T} denotes transpose. Data

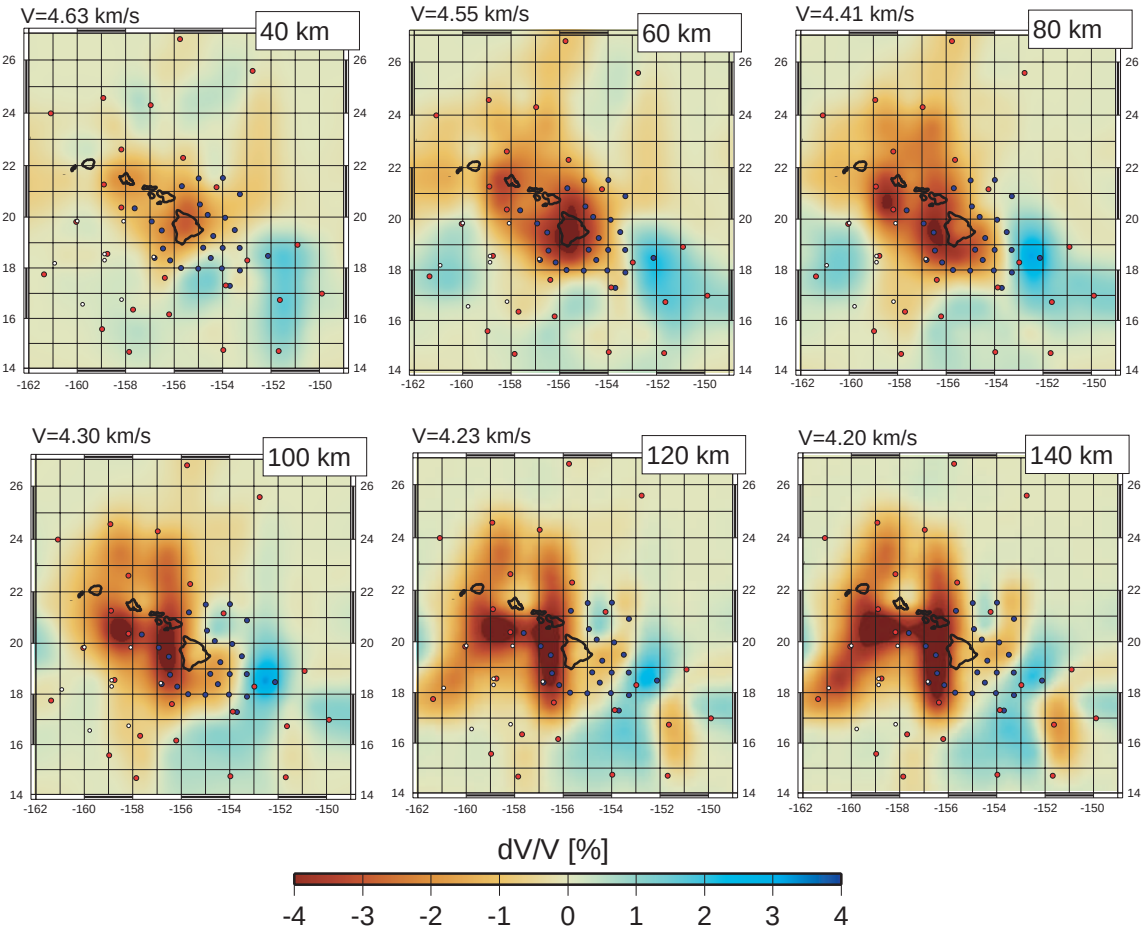

Figure A8. Model of shear velocity anomaly, dV_S/V_S, obtained with approach A. See Fig. A4 for details.

and corresponding rows in the kernel matrix are weighted by the inverse squared data errors. In practice, models that are very close to the minimum of equation B.2 are highly oscillatory, and we chose smoother models. Model errors can be obtained from the data errors through a formal singular value decomposition, by Monte Carlo forward modeling, or by evaluation of the models along the data misfit–model roughness trade-off curve (see Laske *et al.* 2007, for details). We performed inversions for each of the 614 two-station paths.

In a set of 17 laterally smoothed Occam's inversions, one for each layer, we used the 614 path-averaged shear velocities to solve for maps of local shear velocity anomalies. The maps are defined in 13×13 1° cells. We weighted the "data" in this inversion (the path-averaged 1-D profiles) by the inverse of the squared average error in the corresponding dispersion curve. Formally, a more appropriate weight would make use of the actual model error resulting from the initial inversion. Experiments with different weighting schemes,

including one that weights all data equally, indicated that all schemes appear to produce models that are similar to the one shown here.

Six of the resulting shear velocity maps are displayed in Fig. A8. As is the case with the inversion for 1-D profiles, there exists a trade-off between model smoothness and data misfit, where the data are now the values from all 1-D profiles at a given depth. The anomalies stay largely in place as we explore the maps along the trade-off curve, but their amplitudes can change markedly, particularly in areas of less data coverage. However, for models near the minimum of the expression in equation B.2, this inversion scheme produces very smooth, small-amplitude models in areas having little or no data coverage.

In the resulting model, a low-velocity anomaly is found at 60 km depth centered on the island of Hawaii. It diminishes rapidly within $\pm$15 km above and below. At greater depth, anomalies are strongly asymmetric with respect to the island chain, and a pronounced low-velocity anomaly is located to the west of the island of Hawaii. A smaller anomaly is found to the southwest of Oahu. Both anomalies persist throughout the asthenosphere, to depths greater than 140 km. Comparable anomalies are not found to the east of the island chain even though Fig. 9 suggests that data coverage is adequate to detect such anomalies should they exist. The velocity anomalies to the west coincide approximately with the low-velocity anomalies found in the SWELL pilot study (Laske *et al.* 2007). Not considering the larger amplitudes, a strong anomaly at 60 km depth in the SWELL model appears to connect to the anomaly in the PLUME model that is centered on Hawaii. At greater depth, the anomalies in the SWELL model appear somewhat stronger than in the PLUME model. A possible explanation for stronger anomalies in the SWELL model could be that, notwithstanding the apparently adequate data coverage for the PLUME model, the relatively coarse 1° parameterization may lead to underestimates of some anomalies.

REFERENCES

Anderson, O.L. & Isaak, D.G., 1995. Elastic constants of mantle minerals at high temperature, in *Mineral Physics and Crystallography, A Handbook of Physical Constants*, ed. Ahrens, T.J., Reference Shelf 2, American Geophysical Union, Washington, D.C., pp. 64–97.

Anderson, O.L., Schreiber, E., Liebermann, R.C. & Soga, M., 1968. Some elastic constant data on minerals relevant to geophysics, *Rev. Geophys.*, **6**, 491–524.

Constable, S.C., Parker, R.L. & Constable, C.G., 1987. Occam's inversion: a practical algorithm for generating smooth models from electromagnetic sounding data, *Geophysics*, **52**, 289–300.

Laske, G., Phipps Morgan, J. & Orcutt, J.A., 2007. The Hawaiian SWELL pilot experiment – Evidence for lithosphere rejuvenation from ocean bottom surface wave data, in *Plates, Plumes and Planetary Processes*, eds. Foulger, G.R. & Jurdy, D.M., Special Paper 430, Geological Society of America, Boulder, Colo., pp. 209–233.

Masters, G., Laske, G., Bolton, H. & Dziewonski, A., 2000. The relative behavior of shear velocity, bulk sound speed, and compressional velocity in the mantle: implications for chemical and thermal structure, in *Earth's Deep Interior: Mineral Physics and Tomography*, eds. Karato, S.-I., Forte, A.M., Liebermann, R.C., Masters, G. & Stixrude, L., Geophys. Monograph 117, American Geophys. Union, Washington, D.C., pp. 63–87.

Nishimura, C.E. & Forsyth, D.W., 1989. The anisotropic structure of the upper mantle in the Pacific, *Geophys. J.*, **96**, 203–229.